NASA CONTRACTOR REPORT 181824

AN ANALYTICAL AND EXPERIMENTAL INVESTIGATION OF EDGE DELAMINATION IN LAMINATES SUBJECTED TO TENSION, BENDING, AND TORSION

Wen S. Chan
Contract NAS1-18199
Bell Helicopter Textron Inc.

MARCH 1989

National Aeronautics and
Space Administration

Langley Research Center
Hampton, Virginia 23665-5225

AN ANALYTICAL AND EXPERIMENTAL INVESTIGATION OF EDGE DELAMINATION IN LAMINATES SUBJECTED TO TENSION, BENDING, AND TORSION

BHTI Report No. 699-099-265

FINAL REPORT

March 1989

Prepared under Contract NAS1-18199 for the
National Aeronautics and Space Administration

CONTENTS

Page

LIST OF FIGURES v
LIST OF TABLES viii
LIST OF SYMBOLS ix
SUMMARY xiii
FOREWORD xv
INTRODUCTION 1
INTEGRATED FINITE-ELEMENT ANALYSIS FOR FREE-EDGE PROBLEM 3
Finite-Element Formulation 3
Displacement Function 3
Equilibrium Statement 8
Representation of Loading Terms 10
Boundary Conditions 11
Verification of Bending Capability 12
Finite-Element Results 12
Parametric Study 13
Effect of Poisson's Ratio Mismatch 13
Effect of Stacking Sequence 18
Comparison of Present Results 21
Height of Vertical Delamination Opening vs Strain Energy Release Rates .. 24
Delamination Length vs Strain Energy Release Rates 25
Effect of Hybrid Laminate 27
Preliminary Results on Torsion 32
EXPERIMENTS 33
Static and Fatigue Test Matrix 33
Coupon Preparation and Geometry 34
Test Procedure 35
Static Tests 35
Fatigue Tests 37

LIST OF FIGURES

		Page
1	Schematic of a quasi three-dimensional finite-element model	4
2	Variation of interlaminar normal stress σ_{zz} with y at 0/90 interface under bending load	14
3	Variation of interlaminar shear stress σ_{yz} with y at 0/90 interface under bending load	14
4	Variation of interlaminar normal stress σ_{zz} with y at z/H = 2 for $[0_2/\theta_2]_S$ laminates under bending load	16
5	Variation of Poisson's ratio ν_{xy} with θ in T300/5208 graphite/epoxy laminate	16
6	Variation of interlaminar normal stress σ_{zz} through-the-thickness for $[0_2/\theta_2]_S$ laminates at (b - y)/H = 1 under bending load	17
7	Variation of interlaminar shear stress σ_{yz} with y at z/H = 2 for $[0_2/\theta_2]_S$ laminates under bending load	17
8	Variation of interlaminar shear stress σ_{yz} through-the-thickness for $[0_2/\theta_2]_S$ laminates at (b - y)/H = 1 under bending load	18
9	Effect of stacking sequence on interlaminar normal stress in laminates subjected to bending	19
10	Effect of stacking sequence on interlaminar shear stress in laminates subjected to bending	20
11	Effect of stacking sequence on interlaminar normal stress σ_{zz} through-the-thickness at (b-y)/H = 1 for IM6/3501-6 laminates under bending load	22
12	Effect of stacking sequence on interlaminar shear stress σ_{yz} through-the-thickness at (b-y)/H = 1 for IM6/3501-6 laminates under bending load	22
13	Comparison of results for interlaminar shear stress σ_{yz} at z/H = 4 for the $[0_8/90_4]_S$ laminates under bending load	23
14	Comparison of results for interlaminar shear stress σ_{yz} at z/H = 4 for the $[0_8/90_4]_S$ laminates under tension load	23
15	Comparison of present model and Rehfield's results for strain energy release rates in $[0_8/90_4]_S$ T300/5208 laminates under bending load	24

LIST OF FIGURES (Continued)

		Page
16	Change in strain energy release rates with increasing delamination length for a $[90_4/0/\pm45]_S$ IM6/3501-6 graphite/epoxy laminate	26
17	Forces and displacements used in calculation of strain energy release rates for $[90_4/0/\pm45]_S$ IM6/3501-6 graphite/epoxy laminate	26
18	Comparison of strain energy release rates at various interfaces for the $[\pm45/0/90]_S$ laminates, with and without the hybridizing 90° ply	27
19	Comparison of strain energy release rates at various interfaces for the $[0/90/\mp45]_S$ laminates, with and without the hybridizing 90° ply	28
20	Comparison of strain energy release rates at various interfaces for the $[\mp45/90/0]_S$ laminates, with and without the hybridizing 90° ply	28
21	Variation of strain energy release rates at various interfaces for the $[30/-60/-15/75]_S$ laminates	29
22	Variation of strain energy release rates at various interfaces for the $[15/-75/-30/60]_S$ laminates	30
23	Variation of strain energy release rates at various interfaces for the $[15/-75/-60/30]_S$ laminate	31
24	Variation of strain energy release rates at various interfaces for the $[-30/60/-75/15]_S$ laminate	32
25	Coupon configurations for edge-delamination tension test	36
26	Setup for static tests	37
27	Typical load-strain curve for Mode I edge-delamination coupon	39
28	Delamination growth in Mode I coupons during fatigue testing with $\sigma_{max} = 0.90\,\sigma_o$	41
29	Delamination growth in Mode I coupons during fatigue testing with $\sigma_{max} = 0.85\,\sigma_o$	42
30	Delamination growth in Mode I coupons during fatigue testing with $\sigma_{max} = 0.75\,\sigma_o$	43
31	Effect of load level on fatigue life of Mode I edge-delamination glass/epoxy coupons	45

LIST OF FIGURES (Concluded)

		Page
32	Effect of load level on fatigue life of mixed-mode edge-delamination glass/epoxy coupons	49
33	Mixed-mode edge-delamination glass/epoxy coupon after 5,000 and 100,000 cycles	50
34	Effect of load level on fatigue life of mixed-mode edge-delamination graphite/epoxy coupons	53
35	Effect of load level on fatigue life of mixed-mode edge-delamination graphite/glass hybrid coupons	54
36	Comparison of 1- and 5-Hz baseline and hybrid graphite coupons after 100,000 cycles under 90% load	55
37	Comparison of 1-Hz baseline and hybrid graphite coupons after 100,000 cycles under 75% load	56

LIST OF TABLES

		Page
1	Comparison of displacement field formulations	7
2	Comparison of strains corresponding to displacement field formulations	7
3	Material constants	13
4	Effect of stacking sequence on strain energy release rates of S2/SP250 laminates	21
5	Effect of vertical cracking opening height on $[90_4/0/\pm45]_S$ IM6/3501-6 laminate with $K_x = 0.1$	25
6	Strain energy release rates for laminates subjected to a 0.1 twisting curvature	32
7	Coupon test matrix	34
8	Static Mode I edge-delamination test	39
9	Uniaxial material properties for S2/SP250 glass/epoxy laminate	40
10	Fatigue delamination thresholds for Mode I edge-delamination glass/epoxy coupons	44
11	Static test results for mixed-mode edge-delamination coupons	46
12	Fatigue delamination thresholds for mixed-mode edge-delamination glass/epoxy coupons	48
13	Mixed-mode delamination tension test for graphite/epoxy with and without a glass hybridization	51
14	Fatigue delamination thresholds for baseline edge-delamination graphite coupons	51
15	Fatigue delamination thresholds for hybrid edge-delamination graphite/glass coupons	52

LIST OF SYMBOLS

a	delamination length
A_{ij}	extensional stiffness in laminate
b	half-width of coupon
B_{ij}	extension-bending coupling of laminate
[B]	matrix representing partial derivatives of interpolation functions with respect to coordinates
C	twisting curvature [$2C = -2\ (\partial^2 W/\partial x \partial y) = K_{xy}$]
D_{ij}	bending stiffness of laminate
[D]	constitutive matrix
E_1	Young's modulus in fiber direction
E_2	Young's modulus in direction transverse to fiber
E_{lam}	laminate axial stiffness calculated from laminated plate theory
E^*	axial stiffness of a fully delaminated laminate
f	fatigue frequency
{f}	body force intensity vector
{F*}	vector of nodal forces for element
G_{12}	shear modulus in 0° lamina
G_c	interlaminar fracture toughness
G_{IC}	Mode I interlaminar fracture toughness
G_T	total strain energy release rate in laminate
G_I	*opening* component of G_T
G_{II}	*shear* component of G_T
G_{III}	*tearing* component of G_T
h	half of coupon thickness
H	ply thickness
k	longitudinal curvature ($k = -\partial^2 W/\partial x^2 = K_x$)
K_x	curvature in x-direction
K_y	curvature in y-direction
K_{xy}	twisting curvature
M_x	bending moment in x-direction
M_y	bending moment in y-direction

LIST OF SYMBOLS (Continued)

M_{xy}	twisting bending moment
N	total number of elements
N_i	parabolic interpolation functions
N_x^T	laminate resultant load in x-direction due to temperature
N_y^T	laminate resultant load in y-direction due to temperature
$\overline{Q}_{ij}^{k}$	k^{th} ply reduced stiffness
R	fatigue load ratio
(r,s)	element coordinates
t	thickness of laminate
t_i	ply thickness in laminate
t_{ply}	ply thickness in laminate
u(y,z)	element of displacement function in x-direction
U_n	displacement in x-direction for node n, where n = 1, 2, ...8
U(x,y,z)	nodal displacement function in x-direction
{u}	total number of nodal displacements
v(y,z)	element of displacement function in y-direction
V_n	displacement in y-direction for node n, where n = 1, 2, ...8
V(x,y,z)	nodal displacement function in y-direction
w(y,z)	element of displacement function in z-direction
W_n	displacement in z-direction for node n, where n = 1, 2, ...8
W(x,y,z)	nodal displacement function in z-direction
α_1	thermal expansion coefficient in fiber direction
α_2	thermal expansion coefficient in direction transverse to fiber direction
α_i	ply thermal coefficients
$\beta(y)$	angle of rotation
ε_c	axial strain at onset of delamination
ϵ_o	uniform extension (in displacement field)
ϵ_x	strain in x-direction
ϵ_y	strain in y-direction

LIST OF SYMBOLS (Concluded)

ϵ_z	strain in z-direction
ϵ_{yz}	interlaminar shear strain
ϵ_{xy}	in-plane shear strain
$\{\epsilon\}_o$	strain vector
$\{\epsilon\}_L$	strain vector due to load
ν_{12}	Poisson's ratio in 0° lamina
ν_{xy}	Poisson's ratio of laminate
σ_{zz}	interlaminar normal stress in z-direction
σ_{yz}	interlaminar shear stress
Ψ	potential energy due to general applied loads
Ω	strain energy of system

SUMMARY

The objective of this work is to develop an analytical method that can provide insight into the delamination mechanism and to investigate the fatigue delamination characteristics. The approach is to derive a finite-element method, apply the method to layups designed to test the method and to innovative layups designed for improved properties, and then validate by specimen tests.

A simple quasi-three-dimensional finite-element model has been developed to study the free-edge delamination in composite laminates subjected to uniaxial tension, bending, and torsion. This model was used to study laminates with different Poisson's ratios between plies and different stacking sequence. It was found that for a laminate under bending, minimizing the Poisson's ratio difference between plies or stacking the primary load-carrying plies far from the mid-plane can significantly reduce the interlaminar stresses and strain energy release rates. Unlike the tension case, the total strain energy release rate (G_T) and the Mode I strain energy release rate (G_I) for laminates subjected to bending decrease as delamination length increases, reaching a lower bound.

A family of quasi-isotropic graphite/epoxy laminates was investigated to determine the strain energy release rate at various interfaces in the laminate. In addition, a 90° graphite ply was replaced with a glass ply to create a hybrid laminate in the quasi-isotropic layup. A comparison of the strain energy release rates of all-graphite and hybrid layups indicated that the hybrid laminates show a significant reduction in the total strain energy release rate at all the interfaces and in the Mode I strain energy release rate at the 0/90 interface of the various layups.

For the hybrid coupons, a 20% increase in the static onset-of-delamination strength and a 10% increase in ultimate strength resulted from replacing a 90° ply of graphite with a glass ply in the $[\pm 30_2/90_3/\mp 30_2]_T$ graphite laminate. These results confirmed the author's previous work. The test results of all-graphite laminates were included to serve as a baseline for comparison in both static and fatigue tests. For a fatigue life greater than 10^6 cycles, the maximum fatigue load for this type of coupon cannot exceed 59% of the

static onset-of-delamination strength for the baseline coupon and 51% of same delamination strength for the hybrid laminate. It was also found that the hybrid laminate lowers the fatigue delamination onset.

Coupons of S2/SP250 glass/epoxy laminates were tested to establish the delamination onset for Mode I and mixed-mode edge-delamination fatigue fracture. From the Mode I static edge-delamination test, the onset-of-delamination strength was used in the equations to determine interlaminar fracture toughness with and without consideration of the thermal effects of curing. It was found that including the residual stress due to curing increased the interlaminar fracture toughness 125%. The equation developed by Whitney et al. was used to calculate the fracture toughness that included the curing effect. Since the onset of delamination cannot be directly observed in this type of coupon, a delamination length 3% as long as the laminate width was selected as the criterion for the onset of delamination during fatigue. This standard was then used for all the coupons tested in this study and is recommended as superior to a loss-of-stiffness standard.

In both the Mode I and mixed-mode glass/epoxy laminate, the relationship between load and onset of fatigue delamination was established. The test results indicate that to achieve 1×10^6 cycles of fatigue life, the maximum fatigue load cannot be applied above 60% of the static onset-of-delamination load for the Mode I laminates and 43% for the mixed-mode laminates.

FOREWORD

This report describes the development of a finite element model that is capable of identifying the delamination characteristics of laminates under various loadings. Fatigue delamination behavior is also depicted. This work was conducted by Bell Helicopter Textron, Inc. (Bell) between January 1986 and June 1988 in fulfillment of National Aeronautics and Space Administration Contract NAS1-18199. The contract effort was financially supported by the Army Aerostructures Directorate at the Langley Research Center. Dr. T. K. O'Brien was technical monitor.

The project engineer of this program was Dr. Wen S. Chan of the Research Structures Group at Bell. He was assisted in the development of the finite element model by Dr. Ozden O. Ochoa during her leave of absence from Texas A&M University. The coupon test program was performed in the Methods and Materials Laboratory at Bell.

INTRODUCTION

Composite laminate materials have played an important role in the overall improvement of airframe and rotor system structures. One of the most important, yet least understood, factors affecting the strength and durability of composites is interlaminar stress. The flapping capability of the composite rotor, for example, is limited by delamination resulting from the interlaminar stresses at the free edges and ply drops. Improvement in the free-edge delamination strength of composites depends on a fundamental understanding of the delamination characteristics of the structural laminates. Therefore, development of an analytical method that can provide insight into the delamination mechanism under complex loadings is of foremost importance to the analyst.

Early efforts to understand the free-edge delamination problems focused on development of an analytical method to determine interlaminar stresses and strain energy release rates and on investigation into the delamination characteristics of laminates under extension. Pipes and Pagano (1970) solved the elasticity problem by a finite-difference method. Wang and Crossman (1977), using three-noded triangular elements, developed a quasi three-dimensional finite-element approach for modeling the cross sections of laminates. Raju and Crews (1981) took the same approach but used eight-noded isoparametric elements instead. Pagano and Soni (1983) used a global-local model to obtain the interlaminar stress components by lumping plies far from the interface of interest with an equipollent system. Wang and Choi (1982) used Lekhnitskii's stress function and an eigenfunction expansion to obtain a solution for the interlaminar stresses in a laminate. Kassapoglou and Lagace (1985) used the force balance method and the principle of minimum complementary energy to obtain the interlaminar stresses by assuming the shapes of the stresses. Using lamination theory, Sandhu and Sendeckyj (1986) calculated the delaminating moment coefficient as the measure of delaminating tendency of laminates. All the works cited above addressed laminates subjected to extension only.

Salamon (1978) extended Pipes and Pagano's finite-difference method to laminates under pure bending. Armanios and Rehfield (1986) included transverse shear deformation

through rotation, grouped plies together away from the interface of interest, and applied the ply elasticity equation to obtain the stresses between plies. Both tension and bending cases were studied. Their model provided a reasonable estimate for the interlaminar shear components but not for the normal stress component, since no thickness strain was included in the model. No work, to the author's knowledge, has been done on a laminate under torsion.

The strain energy release rate has been widely adopted by analysts because of its success in characterizing delamination. Pagano and Pipes (1973) observed the interlaminar normal stress governing the delamination strength. O'Brien (1980) devised the laminate coupon test to investigate the onset and growth of delamination in graphite/epoxy laminates under uniaxial extension. He developed a simple expression for computing the total strain energy release rate, G_T. The components of the total strain energy release rate, G_I, G_{II}, and G_{III}, associated with opening, shear, and tearing failure modes, respectively, were also based on a quasi three-dimensional finite-element analysis and the crack-closure technique (Rybicki and Kanninen, 1977). Armanios and Rehfield (1986) divided the delaminated region of the laminate and estimated G_T, G_{II}, and G_{III} by the crack-closure method. Then G_I was obtained by subtracting G_{II} and G_{III} from G_T. Only uniaxial extension and bending loads were considered in their studies.

This report covers both the analytical and experimental work performed in a study of the delamination characteristics of laminated composites. In the analytical work, an integrated two-dimensional finite-element model capable of incorporating various loads, including axial, bending, and torsion, is developed to calculate the interlaminar stresses as well as strain energy release rates in laminates. The study addresses the formulation, implementation, and verification of the model. In order to understand delamination characteristics, parametric studies of the effect on interlaminar stress and strain energy release rate of Poisson's mismatch between layers, stacking sequence, delamination length, and delamination opening for various laminates due to bending are included. Preliminary results on laminates subjected to torsion are also included. In the experimental work, fatigue delamination characteristics of graphite/epoxy, glass/epoxy, and their hybrid laminates are investigated. The work is focused on the establishment of fatigue thresholds for Mode I and mixed-mode edge delamination for glass and graphite/glass hybrid laminates.

INTEGRATED FINITE-ELEMENT ANALYSIS FOR FREE-EDGE PROBLEM

A conventional two-dimensional finite-element model is not capable of analyzing the free-edge stress problem, and a full three-dimensional finite-element model is not efficient. Therefore, a quasi three-dimensional finite-element model capable of incorporating various loads, including tension, bending, and torsion, has been developed and is described in this section.

FINITE-ELEMENT FORMULATION

Displacement Function

An isoparametric quadrilateral plate element with eight nodes and three degrees of freedom per node is used to model the cross section of the laminate in the y-z plane (see Figure 1). The displacement field is defined with the customary parabolic interpolation functions N_i, as given below:

$$u(y,z) = \sum_{i=1}^{8} N_i U_i \qquad v(y,z) = \sum_{i=1}^{8} N_i V_i \qquad w(y,z) = \sum_{i=1}^{8} N_i W_i \tag{1}$$

N_i in the element coordinates (r,s) are expressed as

$$\begin{aligned}
N_1 &= \tfrac{1}{4}(1+r)(1+s) - \tfrac{1}{4}(1-r^2)(1+s) - \tfrac{1}{4}(1-s^2)(1+r) \\
N_2 &= \tfrac{1}{2}(1-r^2)(1+s) \\
N_3 &= \tfrac{1}{4}(1-r)(1+s) - \tfrac{1}{4}(1-r^2)(1+s) - \tfrac{1}{4}(1-s^2)(1-r) \\
N_4 &= \tfrac{1}{2}(1-s^2)(1-r) \\
N_5 &= \tfrac{1}{4}(1-r)(1-s) - \tfrac{1}{4}(1-s^2)(1-r) - \tfrac{1}{4}(1-r^2)(1-s) \\
N_6 &= \tfrac{1}{2}(1-r^2)(1-s) \\
N_7 &= \tfrac{1}{4}(1+r)(1-s) - \tfrac{1}{4}(1-r^2)(1-s) - \tfrac{1}{4}(1-s^2)(1+r) \\
N_8 &= \tfrac{1}{2}(1-s^2)(1+r)
\end{aligned} \tag{2}$$

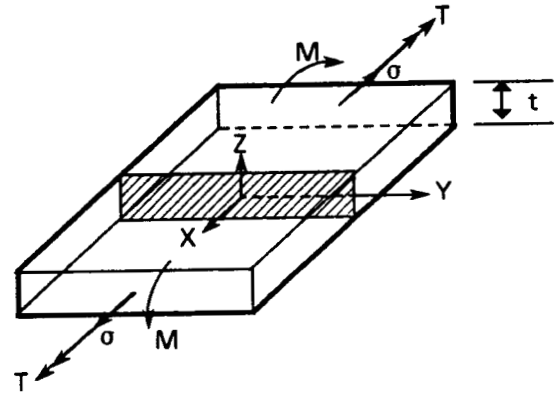

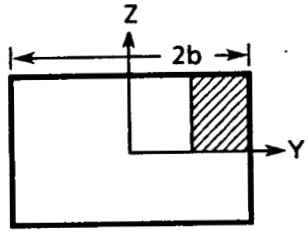

Tension Model

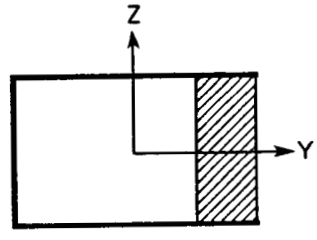

Bending Model

ONLY SHADED AREAS ARE CONSIDERED IN THE FINITE-ELEMENT MODEL.

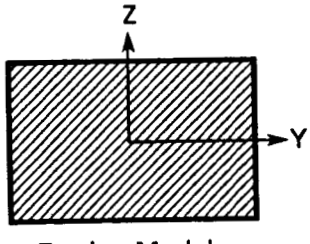

Torsion Model

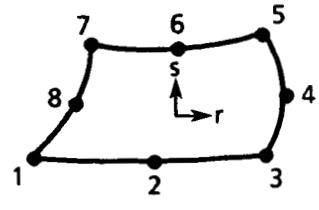

Plate Element with Eight Nodes

Figure 1. Schematic of a quasi three-dimensional finite-element model.

The strain field based on the displacement functions of Eq. (1) takes the following form:

$$\begin{Bmatrix} \epsilon_x \\ \epsilon_y \\ \epsilon_z \\ \epsilon_{yz} \\ \epsilon_{xz} \\ \epsilon_{xy} \end{Bmatrix} = \begin{Bmatrix} \partial u/\partial x \\ \partial v/\partial y \\ \partial w/\partial z \\ \partial v/\partial z + \partial w/\partial y \\ \partial u/\partial z + \partial w/\partial x \\ \partial u/\partial y + \partial v/\partial x \end{Bmatrix} = \underset{6\times 24}{[B]} \quad \underset{24\times 1}{\{u\}} = \{\epsilon\}_o \tag{3}$$

where the [B] matrix represents the partial derivatives of the interpolation functions with respect to coordinates and {u} is the total number of nodal displacements, that is,

$$\{u\} = \begin{Bmatrix} U_1 \\ V_1 \\ W_1 \\ \bullet \\ \bullet \\ \bullet \\ U_8 \\ V_8 \\ W_8 \end{Bmatrix} \tag{4}$$

In order to successfully incorporate "bending" loads into the planar element, the displacement field of Eq. (1) is altered to the following expressions:

$$\begin{aligned} U(x,y,z) &= \epsilon_o x + kxz + u(y,z) \\ V(x,y,z) &= Cxz + v(y,z) \\ W(x,y,z) &= -\tfrac{1}{2}kx^2 - Cxy + w(y,z) \end{aligned} \tag{5}$$

where ϵ_o is the uniform extension, and k and C are the longitudinal and twisting curvatures, respectively, as obtained from

$$K_x = -\frac{\partial^2 W}{\partial x^2} = k \qquad K_y = -\frac{\partial^2 W}{\partial y^2} \qquad K_{xy} = -2\frac{\partial^2 W}{\partial x \partial y} = 2C \tag{6}$$

Thus, a constant bending curvature through the laminate thickness is enforced without bending-extension coupling. It is also noteworthy to look into the case of applying pure twisting curvature, which represents the pure torsion load. For this case K_{xy} (i.e., C) will have a prescribed value where ϵ_o and k of Eq. (5) can be expressed as

$$\{\epsilon\} = \{\epsilon\}_o + \{\epsilon\}_L \tag{7}$$

with $\{\epsilon\}_o$ being the strain vector of Eq. (3) and $\{\epsilon\}_L$ being defined as

$$\{\epsilon\}_L = \begin{Bmatrix} kz + \epsilon_o \\ 0 \\ 0 \\ 0 \\ -Cy \\ Cz \end{Bmatrix} \tag{8}$$

It is important to reference two other displacement fields proposed for the bending problem, namely, those of Armanios and Rehfield (1986), and Ye and Yang (1986). The approach of Ye and Yang, formulated independently of the present authors' work, modifies the displacement field of the same eight-noded isoparametric element to incorporate longitudinal curvature only. The induced twist of laminates that bending contributed to the displacement was totally neglected. Therefore, their model can only be applied to the [0/90] type of laminates. The displacement field suggested by Rehfield is used in a closed-form solution rather than in a finite-element solution and includes a shear deformation through the rotation $\beta(y)$ (see Table 1). Comparisons of the three different displacement formulations and the corresponding strains are presented in Tables 1 and 2, respectively. It is immediately apparent that the present formulation extends itself to torsion problems, in addition to bending problems. The presence of zero strains, i.e., $\epsilon_z = \epsilon_{xy} = \epsilon_{xz} = 0$, in the Rehfield approach is not desirable for accurate presentation of deformation.

TABLE 1. COMPARISON OF DISPLACEMENT FIELD FORMULATIONS

Displacements	Chan & Ochoa	Ye & Yang	Rehfield
U	$u(y,z) + kxz + \epsilon_0 x$	$u(y,z) + kxy$	kxz
V	$v(y,z) + Cxz$	$v(y,z)$	$v(y) + z\beta(y)$
W	$w(y,z) - \frac{1}{2}kx^2 - Cxy$	$w(y,z) - \frac{1}{2}kx^2$	$w(y) - \frac{1}{2}kx^2$

TABLE 2. COMPARISON OF STRAINS CORRESPONDING TO DISPLACEMENT FIELD FORMULATIONS

Strains	Chan & Ochoa	Ye & Yang	Rehfield
ϵ_x	$\epsilon_0 + kz$	kz	kz
ϵ_y	$\frac{\partial v}{\partial y}$	$\frac{\partial v}{\partial y}$	$\frac{\partial v}{\partial y} + \frac{z d\beta}{dy}$
ϵ_z	$\frac{\partial w}{\partial z}$	$\frac{\partial w}{\partial z}$	0
ϵ_{xy}	$\frac{\partial u}{\partial y} + Cz$	$\frac{\partial u}{\partial y}$	0
ϵ_{xz}	$\frac{\partial u}{\partial z} - Cy$	$\frac{\partial u}{\partial z}$	0
ϵ_{yz}	$\frac{\partial v}{\partial z} + \frac{\partial w}{\partial y}$	$\frac{\partial u}{\partial z} + \frac{\partial w}{\partial y}$	$\beta + \frac{dw}{dy}$

Equilibrium Statement

The present finite-element model formulation is based on the minimization of total potential energy. The strain energy of the system (all assembled elements) is expressed as

$$\Omega = \frac{1}{2} \sum_{e=1}^{N} \int_{vol} \{\sigma\}^T \{\epsilon\} dVol \tag{9}$$

where N is the total number of elements and the volume integral is over an element or with the use of the constitutive relations

$$\Omega = \sum_{e=1}^{N} \int_{vol} \frac{1}{2} \{\epsilon\}^T [D] \{\epsilon\} \, dVol \tag{10}$$

Substituting Eq. (7) into Eq. (10) yields

$$\Omega = \sum_{e=1}^{N} \int \frac{1}{2} \left(\{\epsilon\}_o^T + \{\epsilon\}_L^T \right) [D] \left(\{\epsilon\}_o + \{\epsilon\}_L \right) dVol \tag{11}$$

Upon rearranging terms,

$$\Omega = \sum_{e=1}^{N} \int_{vol} \frac{1}{2} \left(\{\epsilon\}_o^T [D] \{\epsilon\}_o + \{\epsilon\}_o^T [D] \{\epsilon\}_L \right.$$

$$\left. + \{\epsilon\}_L^T [D] \{\epsilon\}_o + \{\epsilon\}_L^T [D] \{\epsilon\}_L \right) dVol \tag{12}$$

Now, recall that from Eq. (3), $\{\epsilon\}_o$ can be represented by

$$\{\epsilon\}_o = [B] \{\bar{u}\} \tag{13}$$

Substituting Eq. (13) into Eq. (12) and collecting terms yields

$$\Omega = \sum_{e=1}^{N} \int_{Vol} \frac{1}{2} \left(\{\bar{u}\}^T [B]^T [D][B]\{\bar{u}\} + \{\bar{u}\}^T [B]^T [D]\{\epsilon\}_L \right.$$

$$\left. + \{\epsilon\}_L^T [D][B]\{\bar{u}\} + \{\epsilon\}_L^T [D]\{\epsilon\}_L \right) dVol \tag{14}$$

On the other hand, the potential energy due to the general applied loads is

$$\Psi = \sum_{e=1}^{N} \int - \{\bar{u}\}^T \{f\}\, dVol \tag{15}$$

Thus, the total potential energy is obtained by the summation of Eqs. (14) and (15). The minimization of the total potential energy with respect to the nodal displacements (generalized coordinates) provides the equilibrium statement for the system, that is,

$$\frac{\partial \Pi}{\partial \bar{u}} = \frac{\partial(\Omega + \Psi)}{\partial \bar{u}} = 0 \tag{16}$$

The resulting equilibrium statement, in terms of the stiffness matrix and the load vector, is presented below:

$$\underbrace{\left(\sum_{e=1}^{N} \int_{Vol} [B]^T [D][B]\, dVol \right) \{\bar{u}\}}_{[K]} + \underbrace{\left(\sum_{e=1}^{N} \int_{Vol} [B]^T [D]\{\epsilon\}_L\, dVol \right)}_{\text{Contribution from the loading terms}} = \underbrace{\sum_{e=1}^{N} \int_{Vol} \{f\} dVol}_{\{f\}} \tag{17}$$

[K]
Stiffness matrix for the assembled system

Contribution from the loading terms

{f}
Acting on the system in general

The second term on the left side of Eq. (17) is obtained from the contributions of the curvatures included in the displacement field of Eq. (5).

Then, the final form of the equilibrium statement is given as

$$\left(\sum_{e=1}^{N}\int_{Vol}[B]^T[D][B]\,dVol\right)\{\bar{u}\} = \sum_{e=1}^{N}\int_{Vol}\left(\{f\}-[B]^T[D]\{\epsilon\}_L\right)dVol \tag{18}$$

or, in short,

$$[K]\{u\} = \{F^*\} \tag{19}$$

As can be observed, the effect of curvature can be interpreted as a "bending load" effect. Therefore, one does not need to re-evaluate the stiffness matrix for the isoparametric element with an extensional displacement field, as given in Eq. (1). The bending effect can simply be incorporated by redefining the load vector, as shown in Eqs. (18) and (19).

Representation of Loading Terms

From classical lamination theory, the moments can be expressed as

$$M_x = B_{11}\epsilon_o + D_{11}k + D_{12}K_y + 2D_{16}C \tag{20}$$

$$M_y = B_{12}\epsilon_o + D_{12}k + D_{22}K_y + 2D_{26}C \tag{21}$$

$$M_{xy} = B_{16}\epsilon_o + D_{16}k + D_{26}K_y + 2D_{66}C \tag{22}$$

where ϵ_o is elongation in the x-direction, and k, K_y, and C are the curvatures about x, y, and the twisting axes, respectively. Positive sign convention for k is concave downward.

For a problem of pure bending about the x axis, $M_y = M_{xy} = 0$. Therefore, simultaneous solutions of Eqs. (21) and (22) yield the expression for 2C (twisting curvature) as a function of k (longitudinal curvature) and ϵ_o (elongation):

$$2C = \frac{1}{D_{22}D_{66} - D_{26}^2}\left[\epsilon_o\left(B_{12}D_{26} - B_{16}D_{22}\right) + k\left(D_{12}D_{26} - D_{16}D_{22}\right)\right] \tag{23}$$

For symmetric laminates under pure bending, the above expression reduces to

$$2C = \frac{1}{D_{22}D_{66} - D_{26}^2} k\left(D_{12}D_{26} - D_{16}D_{22}\right) \tag{24}$$

Then, the strain field obtained from the bending contributions, $\{\epsilon\}_L$, can be expressed as a function of k, only, by substituting Eq. (24) into (8).

A similar discussion is valid for pure torsion load about the x axis with $M_x = M_y = 0$. Then, for a prescribed value of C, k and K_y are given as

$$k = -2C\left(\frac{D_{16}D_{22} - D_{12}D_{26}}{D_{22}D_{12} - D_{12}^2}\right) \tag{25}$$

$$K_y = -2C\left(\frac{D_{11}D_{26} - D_{12}D_{16}}{D_{22}D_{11} - D_{12}^2}\right) \tag{26}$$

It should be noted that the bending stiffness, D_{ij}, used here was obtained from lamination theory for laminates with no delamination. To account for laminates with edge delamination, the bending stiffness should be re-evaluated.

Boundary Conditions

Because of symmetries inherent in the laminates under consideration and in the loading condition across the cross section, the region to be modeled is dependent on the loading case. The three cases, shown in Figure 1, are modeled as follows:

Uniaxial loading	A portion of the quarter cross section close to the free edge, where interlaminar stress exists, is modeled with symmetric boundary conditions imposed along the y and z axes.
Bending	The total through-the-thickness direction is modeled with symmetric boundary conditions imposed about the z axis.
Torsion	The entire cross section is modeled, creating antisymmetric displacements and stresses.

The origin of the modeled region is constrained against any displacement, i.e., $u(0,0) = v(0,0) = w(0,0) = 0$.

VERIFICATION OF BENDING CAPABILITY

A thick laminate, $[0/90_2/0]_{16S}$, 1 in. wide and 0.64 in. thick, was modeled with 120 elements. The material was T300/5208, with the properties shown in Table 3. The z axis was taken as an axis of symmetry; thus, only a half-width of the laminate was modeled. The applied loading was in the form of prescribed curvature $K_x = k = 0.1$. The outermost layers were 0.02 in. thick, which is 6.25% of the total laminate thickness. This geometry and the loading conditions ensured the existence of uniform stress-strain fields in the outermost thin layers. To assess the results obtained from the computer program for the bending load, another model was used to obtain the stress field for a thin $[0/90]_S$ laminate, 0.02 in. thick (same thickness as the outermost layer of the thick laminate), subjected to uniaxial tension. Figures 2 and 3 show, respectively, the normal and shear stresses obtained from the bending model and the uniaxial tension model at the upper 0/90 interface. The good agreement between the two models lends confidence in the programming of the bending subroutine developed for the computer code.

FINITE-ELEMENT RESULTS

In this section, the finite-element code based on the formulation described in the previous section is verified. The computer code is then used to investigate the effect of interlaminar stresses resulting from a Poisson's ratio mismatch between plies and the

stacking sequences in laminates, and the effect on strain energy release rate of changes in the magnitude of delamination openings and delamination sizes. A comparison of the present model with the approximate closed-form model is presented. The effect of strain energy release rate in hybrid laminates is also discussed.

To determine the strain energy release rate, the bending stiffness used was calculated from the laminate with no delamination, since the length of the delamination considered in this study was small compared to the laminate width.

The material constants for the laminates used in this study are listed in Table 3.

TABLE 3. MATERIAL CONSTANTS

Parameter	IM6G/3501-6	S2/SP250	S2/CE9000	T300/5208
E_1	24.8 Msi	7.3 Msi	8.09 Msi	20.0 Msi
E_2	1.41 Msi	2.1 Msi	2.28 Msi	2.1 Msi
G_{12}	0.9 Msi	0.88 Msi	1.06 Msi	0.85 Msi
ν_{12}	0.329	0.275	0.288	0.21
t_{ply}	0.0074 in.	0.0085 in.	0.0074 in.	0.005 in.

Parametric Study

The investigation of interlaminar stresses resulting from different Poisson's ratios between plies and from different stacking sequences is described below.

Effect of Poisson's Ratio Mismatch

The difference in Poisson's ratio mismatch between plies has a significant effect on interlaminar stresses of laminates subjected to tension (Chan et al., 1986). To study this effect on interlaminar stresses of laminates subjected to bending, a series of T300/5208 laminates with a $[0_2/\theta_2]_S$ layup were used. The θ was varied from 30° to 90° in increments of 15°. The applied loading was in the form of prescribed curvature $K_x = k = 0.1$.

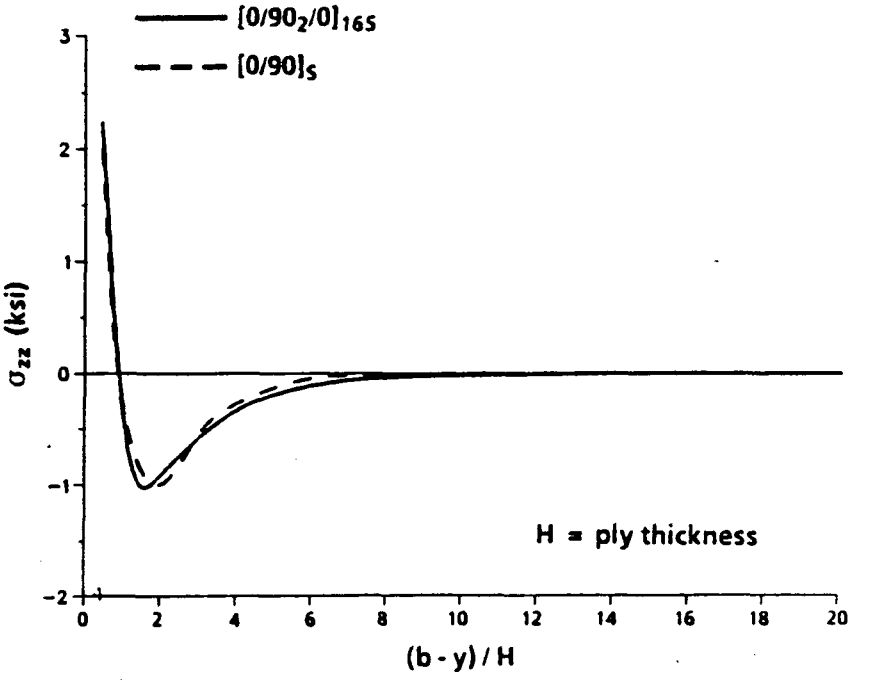

Figure 2. Variation of interlaminar normal stress σ_{zz} with y at 0/90 interface under bending load.

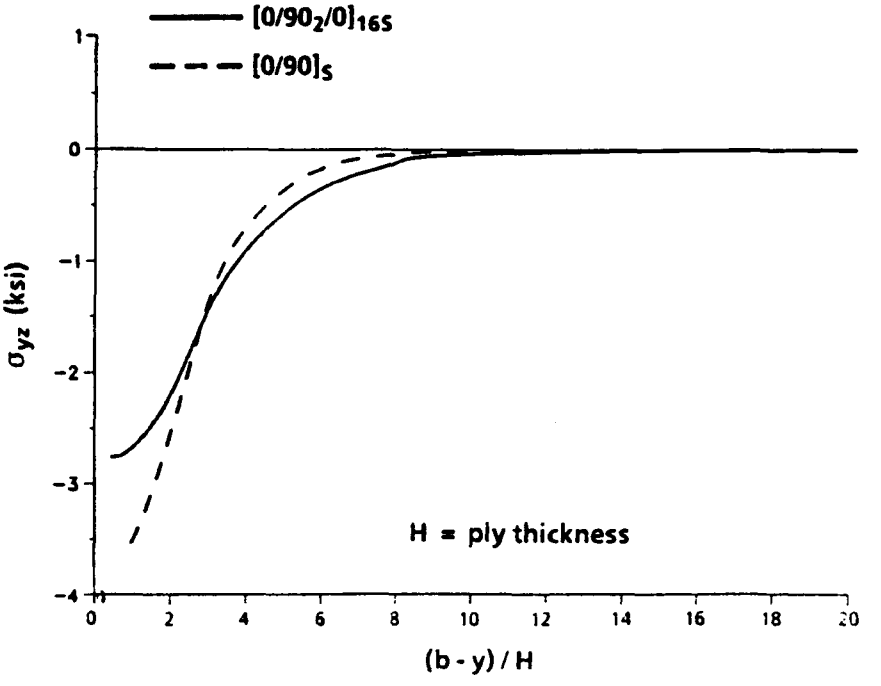

Figure 3. Variation of interlaminar shear stress σ_{yz} with y at 0/90 interface under bending load.

Figure 4 shows the distribution of normal stress, σ_{zz}, across the width at the upper 0/θ interface of the $[0_2/\theta_2]_S$ laminates where the 0° plies exhibit positive longitudinal stress (σ_x). As shown in the figure, the laminates with θ = 90° and 75° give rise to an interlaminar normal tensile stress at the free edge. However, the laminates with θ = 15°, 30°, 45°, and 60° have an interlaminar normal compressive stress at the edges. The tensile and compressive interlaminar normal stresses at the free edge can be explained by the difference in Poisson's ratio between the plies.

The variation in Poisson's ratio with respect to the fiber orientation of the material considered in this study is depicted in Figure 5. For the θ = 90° or 75° laminate, there is less deformation in the transverse direction than in its neighboring 0° ply, so the edges of the laminate at this interface tend to curve away from the midplane of the laminate. As a result, interlaminar normal tensile stress is induced. For θ = 60° or less, the edges of the laminate at the upper 0/θ interface curve inward, since the less deformed 0° ply opposes the effort of its neighboring ply to curve outward, and the result is compressive stress in the thickness direction. It is noted that at the lower 0/θ interface, all the stresses will be reversed, since the fiber stress of the 0° plies is under compression.

Figure 6 shows the distribution of interlaminar normal stress, σ_{zz}, through the thickness near the free edge. The figure confirms the zero σ_{zz} at the outer surfaces and at the midplane, where no longitudinal stress exists because of bending. It is also shown that the stress behaves, as expected, as an antisymmetrical distribution.

The interlaminar shear distribution, σ_{yz}, along the upper 0/θ interface for the θ = 30°, 60°, and 90° laminates is shown in Figure 7. In this figure, the maximum peak for interlaminar shear at the 0/θ interface occurs in the θ = 30° laminate, which is the angle where the maximum difference in Poisson's ratio occurs.

The interlaminar shear variation through the thickness near the free edge, illustrated in Figure 8, indicates that the peak values occur at the interface and at the midplane locations.

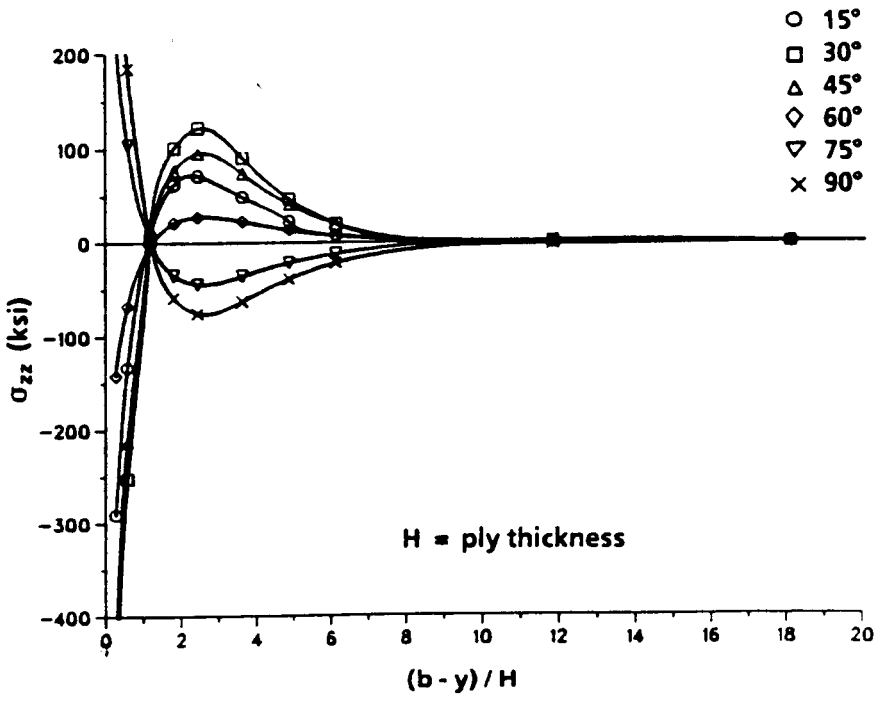

Figure 4. Variation of interlaminar normal stress σ_{zz} with y at z/H = 2 for $[0_2/\theta_2]_S$ laminates under bending load.

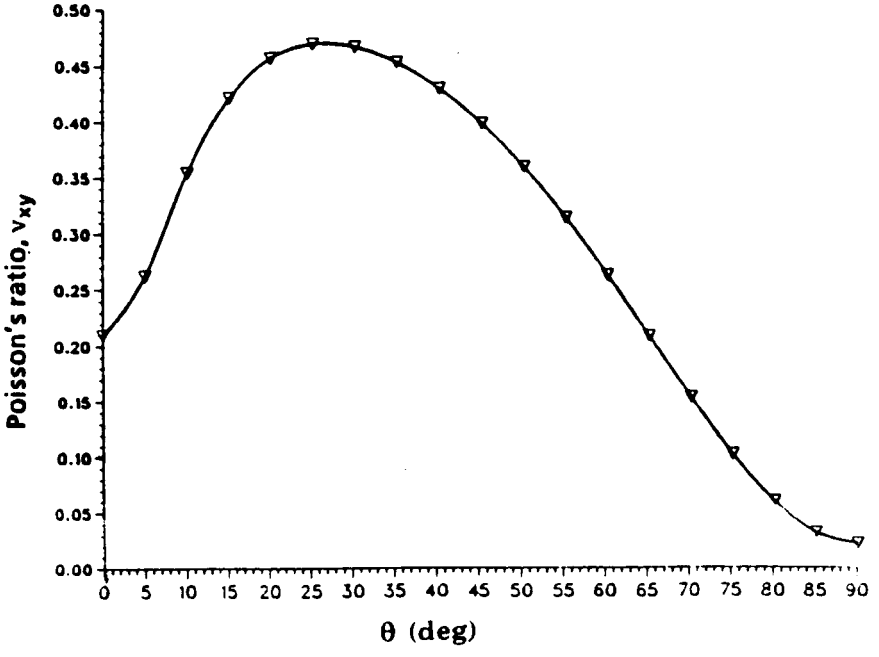

Figure 5. Variation of Poisson's ratio ν_{xy} with θ in T300/5208 graphite/epoxy laminate.

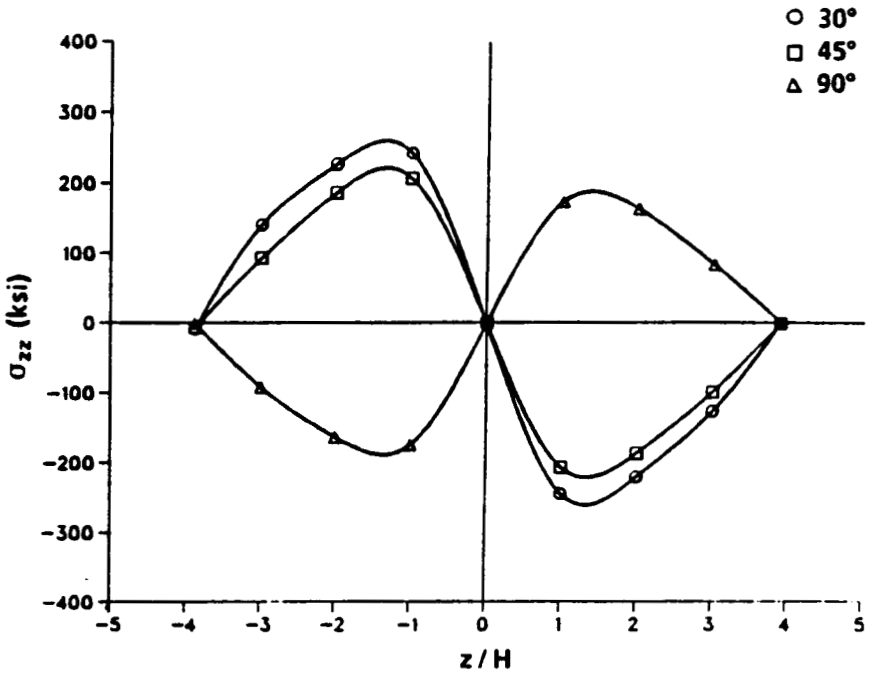

Figure 6. Variation of interlaminar normal stress σ_{zz} through-the-thickness for $[0_2/\theta_2]_S$ laminates at (b - y)/H = 1 under bending load.

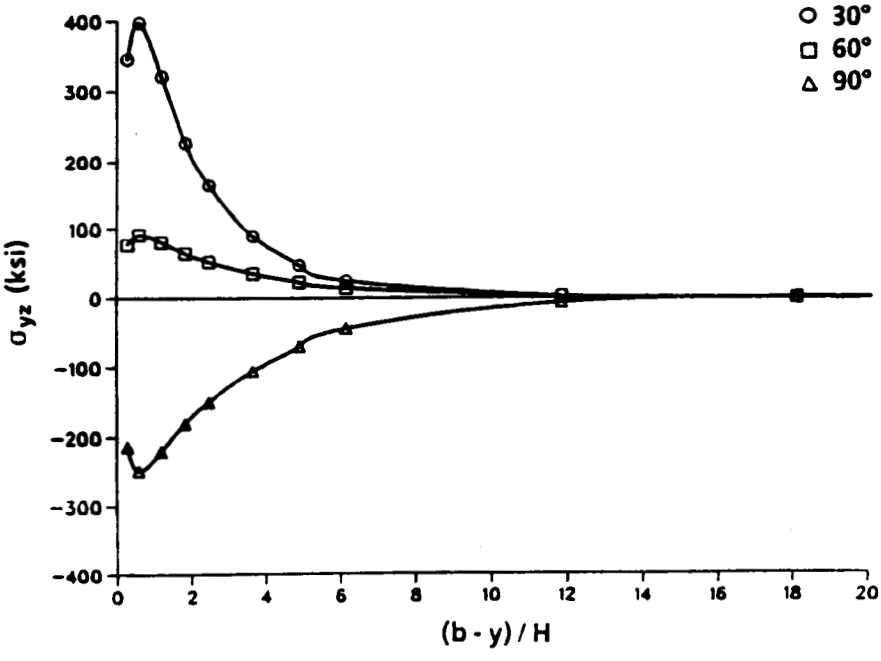

Figure 7. Variation of interlaminar shear stress σ_{yz} with y at z/H = 2 for $[0_2/\theta_2]_S$ laminates under bending load.

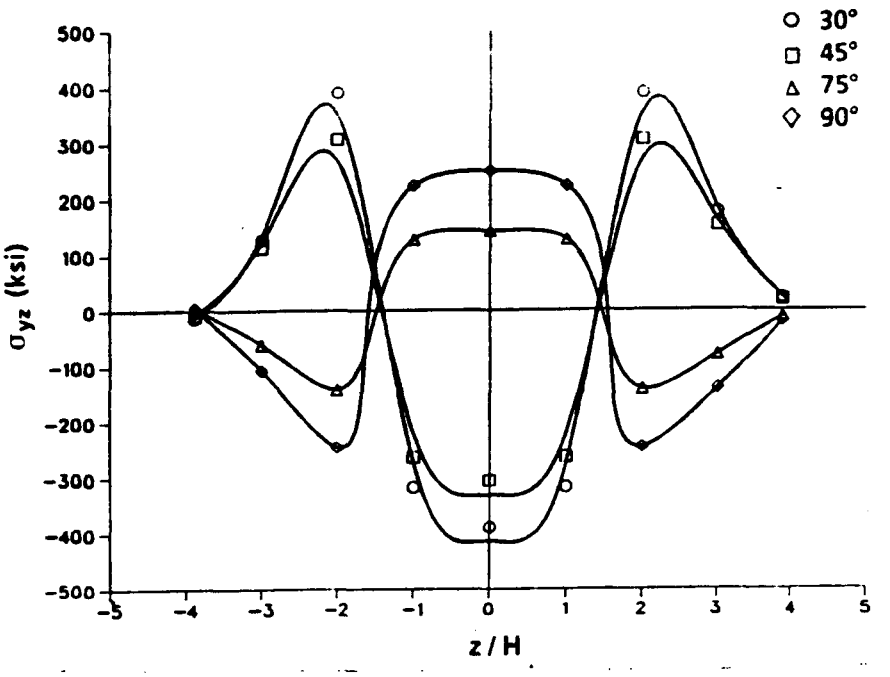

Figure 8. Variation of interlaminar shear stress σ_{yz} through-the-thickness for $[0_2/\theta_2]_S$ laminates at (b - y)/H = 1 under bending load.

Effect of Stacking Sequence

Two families of laminates, $(0_9/\pm45_2)_S$ S2/SP250 glass/epoxy and $(\pm45/0/90)_S$ IM6/3501-6 graphite/epoxy, were used to study the influence of stacking sequence on interlaminar stresses and strain energy release rates. The material constants for these materials are given in Table 3.

Laminates of S2/SP250 glass/epoxy with three different stacking sequences were fabricated: $[0_9/\pm45_2]_S$, $[0_7/\pm45/0/\pm45/0]_S$, and $[0_5/\pm45/0_3/\pm45/0]_S$. The ply thickness, H, was 0.0085 inch. The laminates were subjected to a constant curvature of k = 0.1 and plots made of the resulting interlaminar stresses. These plots, shown in Figures 9 and 10, depict the distribution of normal and shear components, respectively, through the thickness at one ply distance away from the free edge. It is clear that all the peaks for normal stress occur at the first ±45 ply interface from the outer surface of the laminate. However, the peaks for shear are located at the first 0/45 interface from the

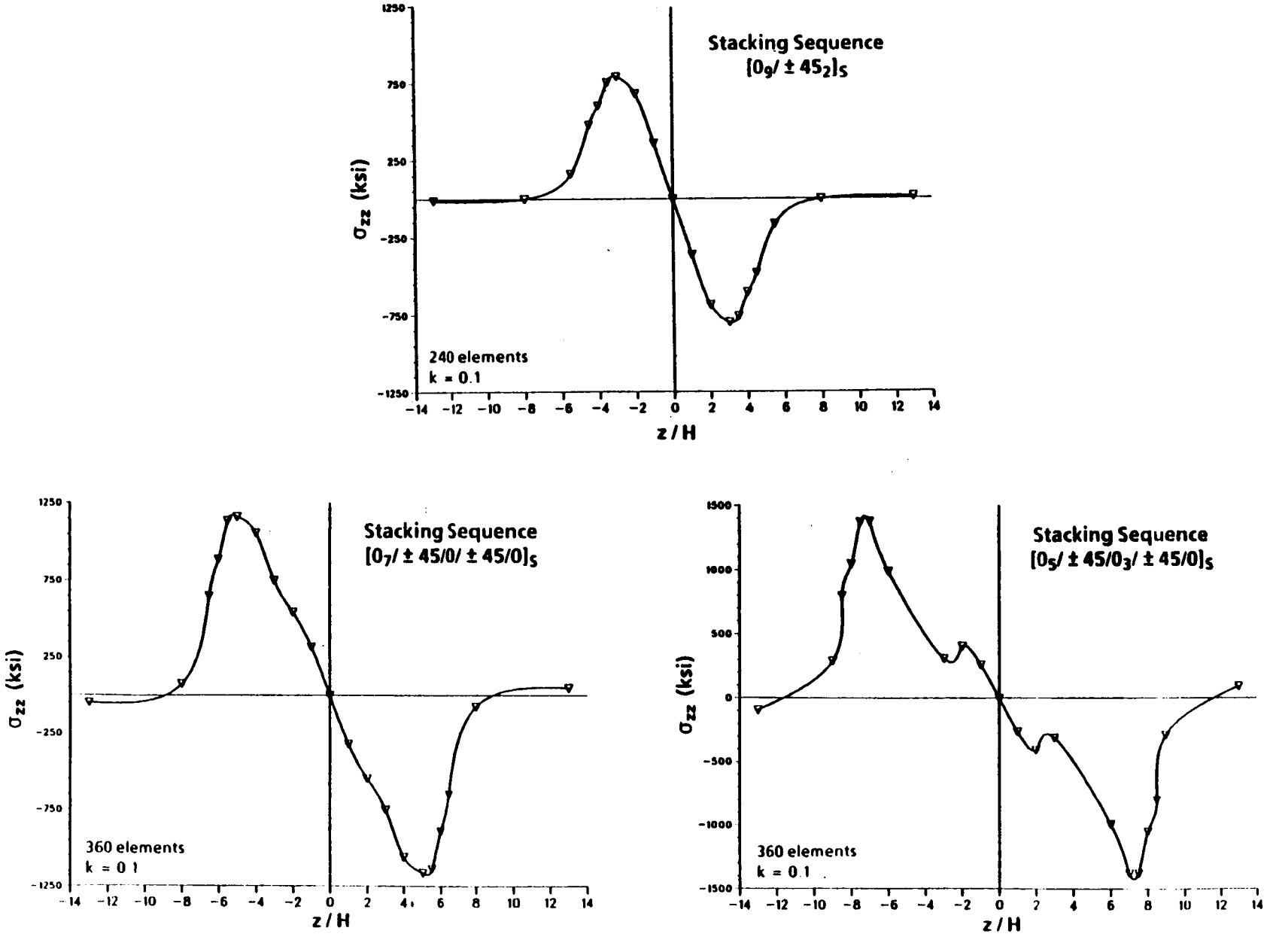

Figure 9. Effect of stacking sequence on interlaminar normal stress in laminates subjected to bending.

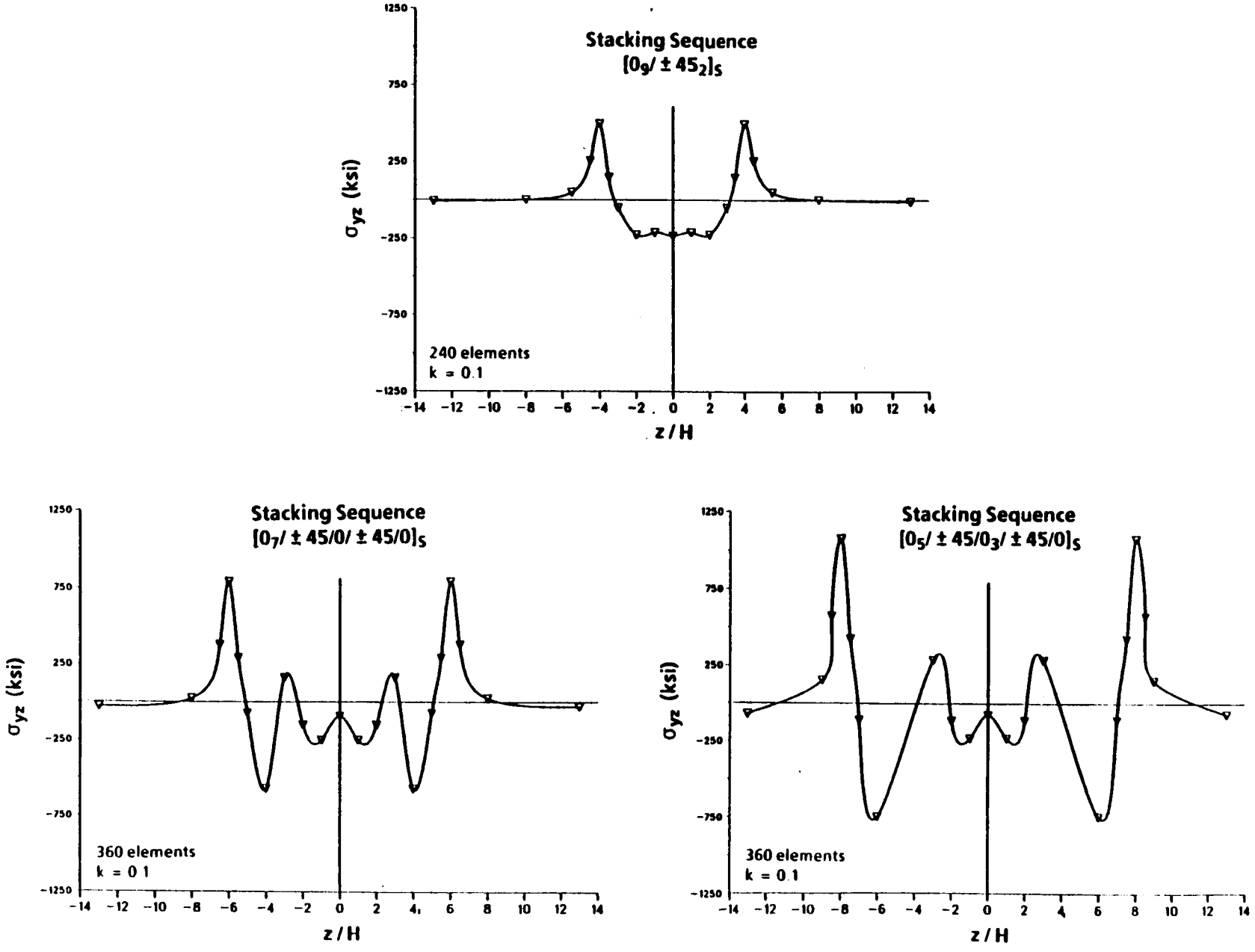

Figure 10. Effect of stacking sequence on interlaminar shear stress in laminates subjected to bending.

outer surface. The results also strongly indicate that, of the three laminates, $[0_9/\pm45_2]_S$ has the smallest peak values for both normal and shear. The calculated strain energy release rates for these three laminates with a delamination at the first 0/45 interface from the bottom surface are shown in Table 4. The results imply that G_I and G_{II}, as well as G_T, can be significantly reduced if all the 0° plies are placed near the outer surface.

TABLE 4. EFFECT OF STACKING SEQUENCE ON STRAIN ENERGY RELEASE RATES OF S2/SP250 LAMINATES[a]

Laminate	Strain Energy Release Rate (in-lb/in^2 x 10^{-3})			
	G_I	G_{II}	G_{III}	G_T
$[0_9/\pm45_2]_S$	3.033	3.471	0.817	7.321
$[0_7/\pm45/0/\pm45/0]_S$	14.170	15.123	1.518	30.811
$[0_5/\pm45/0_3/\pm45/0]_S$	24.196	26.528	1.358	52.082

[a] k = 0.1, a/H = 8. Delamination at first 0/45 interface from bottom.

The stacking sequences for the IM6/3501-6 graphite/epoxy laminates were $[0/\pm45/90]_S$, $[\pm45/0/90]_S$, and $[90/\pm45/0]_S$. The stress fields are displayed in Figures 11 and 12. Figure 11 shows a high peak for σ_{zz} at the (45/-45) interface (z/H = -2) in the $[90/\pm45/0]_S$ laminate. However, a high peak for the shear, σ_{yz}, shown in Figure 12, is located at the 90/45 interface (z/H = ±3) of the $[90/\pm45/0]_S$ laminate.

Comparison of Present Results

The $[0_8/90_4]_S$ laminate of T300/5208 graphite/epoxy studied by Armanios and Rehfield (April 1986) was selected for comparison with the present finite-element results. Since their theory can only provide interlaminar shear, interlaminar normal stress was not considered in this study.

Figures 13 and 14 show the interlaminar shear (σ_{yz}) distribution along the 0/90 interface from the top of the laminate when subjected to bending and tension, respectively. It is

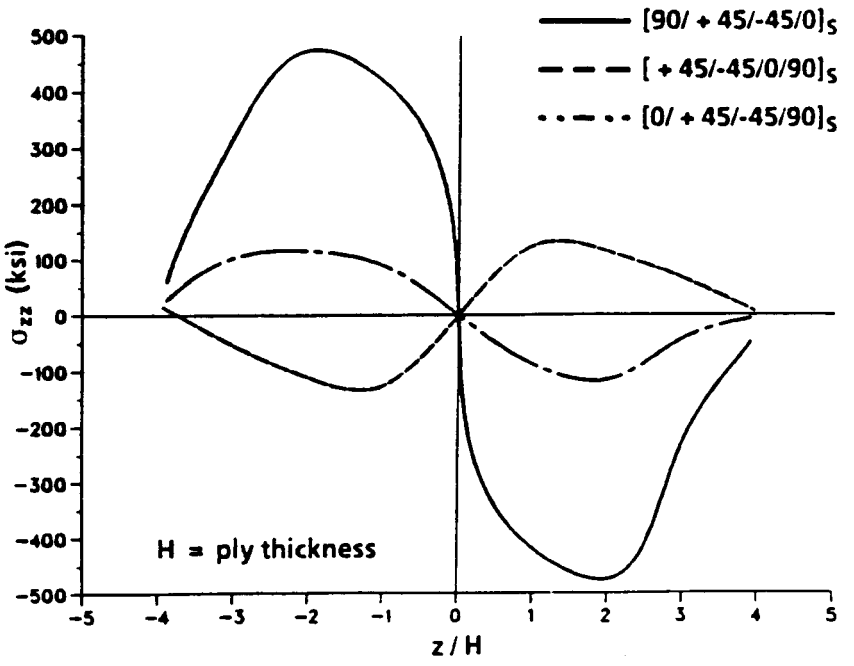

Figure 11. Effect of stacking sequence on interlaminar normal stress σ_{zz} through-the-thickness at (b-y)/H = 1 for IM6/3501-6 laminates under bending load.

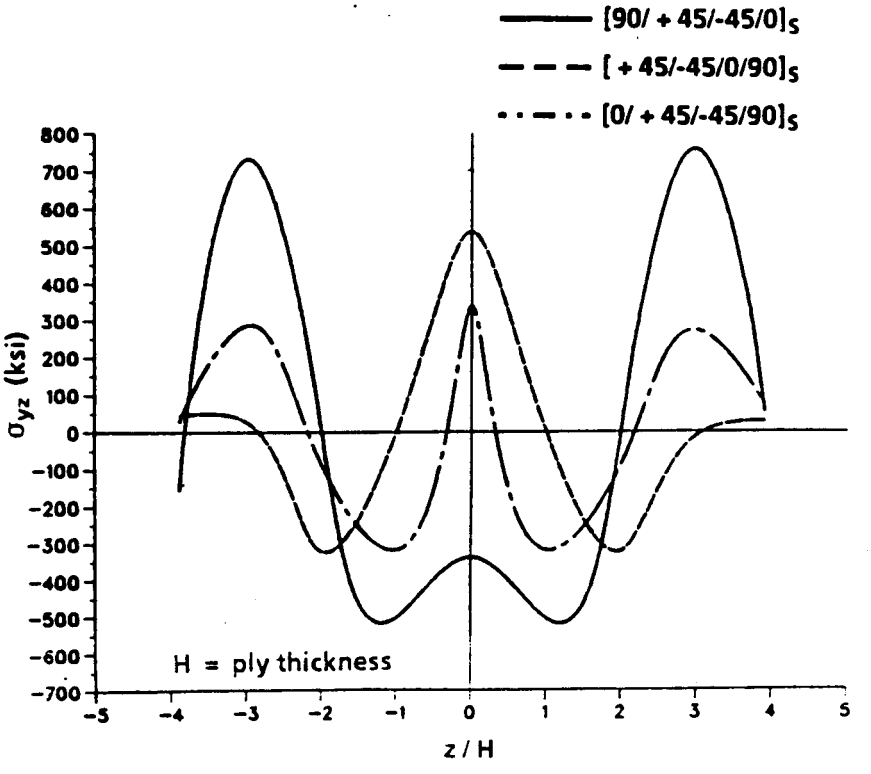

Figure 12. Effect of stacking sequence on interlaminar shear stress σ_{yz} through-the-thickness at (b-y)/H = 1 for IM6/3501-6 laminates under bending load.

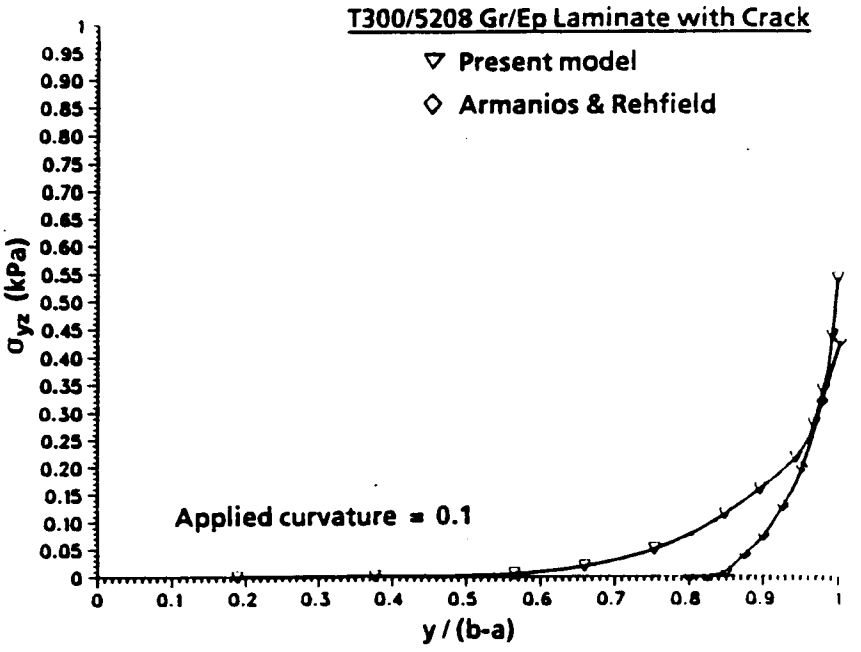

Figure 13. Comparison of results for interlaminar shear stress σ_{yz} at z/H = 4 for the $[0_8/90_4]_S$ laminates under bending load.

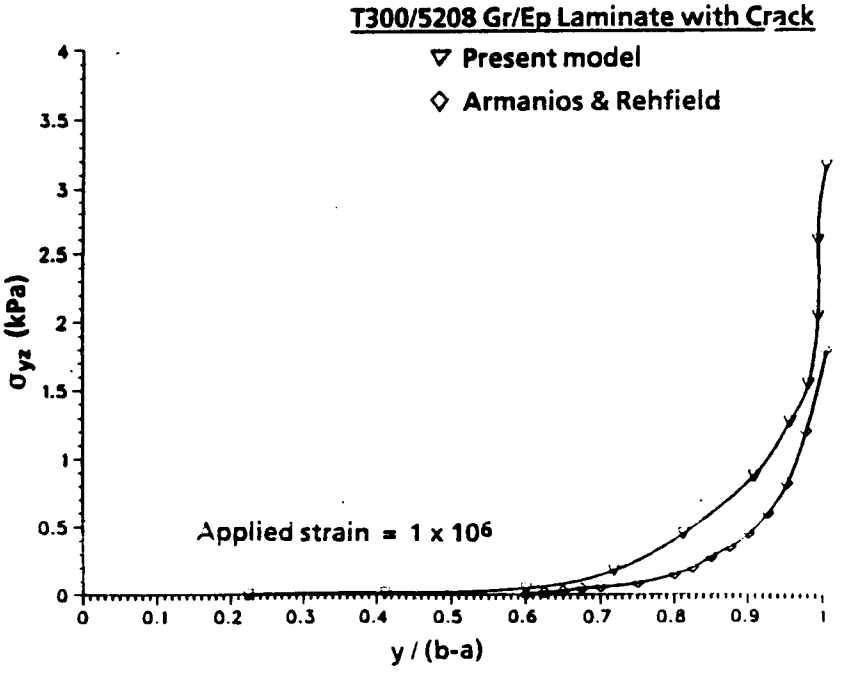

Figure 14. Comparison of results for interlaminar shear stress σ_{yz} at z/H = 4 for the $[0_8/90_4]_S$ laminates under tension load.

noted that the interlaminar shear stress zone depicted by both methods is comparable for laminates subjected to tension. However, the finite-element method predicts a larger zone than Rehfield's method in the case of bending load. This is because the contribution of the shear strain, γ_{yz}, in the z direction to the interlaminar shear, σ_{yz}, is not considered in Rehfield's solution.

Both methods were used to obtain the strain energy release rates of the same laminate. Figure 15 shows that the finite-element results are comparable to Rehfield's results. In both cases the G calculations were based on a delamination having a length of six ply thicknesses located at the 0/90 interface.

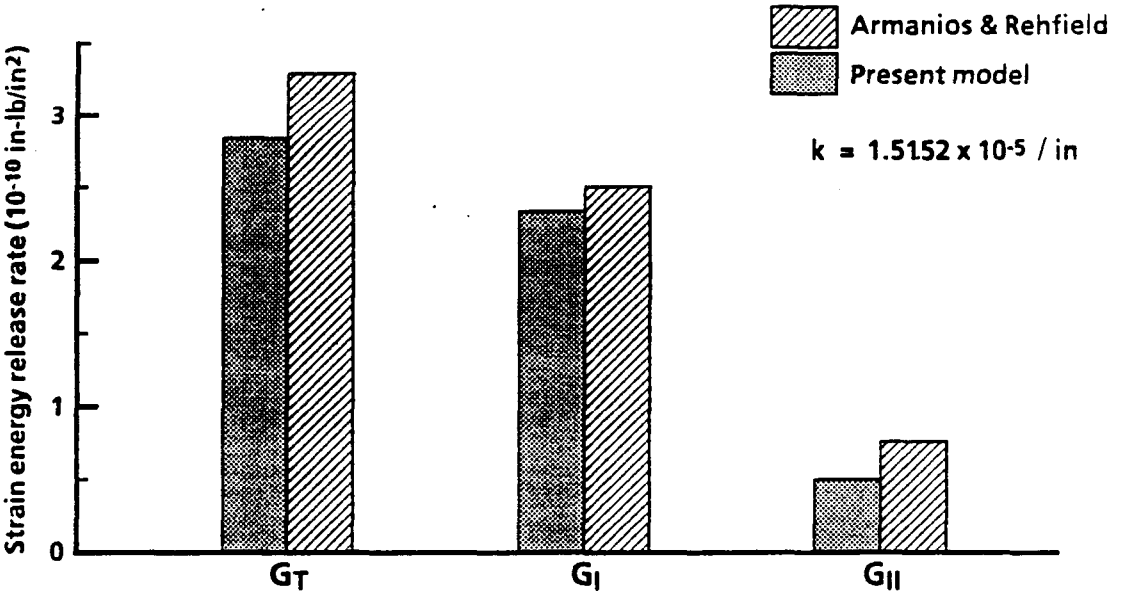

Figure 15. Comparison of present model and Rehfield's results for strain energy release rates in $[0_8/90_4]_S$ T300/5208 laminates under bending load.

Height of Vertical Delamination Opening vs Strain Energy Release Rates

A $[90_4/0/\pm45]_S$ IM6/3501-6 graphite/epoxy laminate was subjected to a constant curvature to study the relationship between strain energy release rate and the height of a vertical (z-direction) delamination opening at the 0/45 interface. Both the opening and the length of the delamination were predetermined in the analysis. Three different opening heights were considered. The results, shown in Table 5, indicate that the height

of the delamination opening has little if any effect on the G calculation. It was therefore concluded that the use of a mathematical crack with zero height to simulate the actual delamination in the analysis would not result in error.

TABLE 5. EFFECT OF VERTICAL CRACK OPENING HEIGHT ON $[90_4/0/\pm45]_S$ IM6/3501-6 LAMINATE WITH $K_x = 0.1$

Crack Opening	G_T (in-lb)/in^2	G_I (in-lb)/in^2	G_{II} (in-lb)/in^2	G_{III} (in-lb)/in^2
0.0 H[a]	12.0×10^{-3}	4.12×10^{-3}	3.22×10^{-3}	4.87×10^{-3}
0.02 H	12.2×10^{-3}	4.12×10^{-3}	3.19×10^{-3}	4.91×10^{-3}
0.1 H	12.2×10^{-3}	4.12×10^{-3}	3.22×10^{-3}	4.89×10^{-3}

[a]Ply thickness

Delamination Length vs Strain Energy Release Rates

To determine how the strain energy release rates change as the length of a delamination increases in the y-direction, a $[90_4/0/\pm45]_S$ laminate of IM6/3501-6 graphite/epoxy was subjected to a constant curvature of k = 0.1. Since the laminate was found to have the highest interlaminar stresses at the lower 0/45 interface prior to delamination, a delamination was assumed to occur at that interface. The results of the calculation are shown in Figure 16. For very short cracks, i.e., a/H = 1 to 5, the behavior of the individual G's does not follow a consistent pattern. However, at a delamination length greater than eight times the ply thickness, the strain energy release rates, G_I, G_{II}, G_{III}, and G_T, level out and become constant in value. This behavior is different from that observed in the tension case. For tension, the strain energy release rate increases as the delamination length increases, reaching a plateau at a certain length. To better understand the G's behavior, the forces and displacements used for G calculation are shown in Figure 17. It is noted that F_z and U_z decrease significantly as delamination length increases.

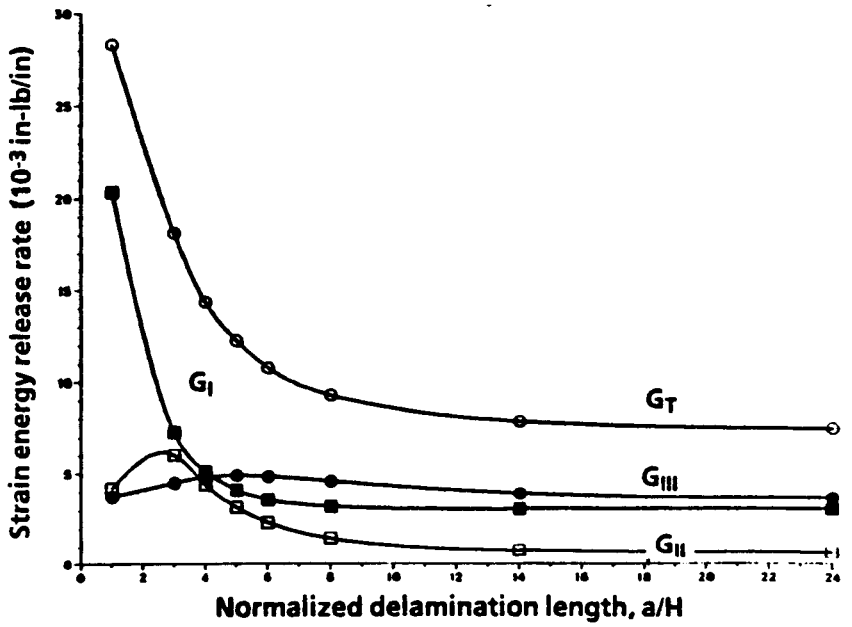

Figure 16. Change in strain energy release rates with increasing delamination length for a $[90_4/0/\pm45]_S$ IM6/3501-6 graphite/epoxy laminate.

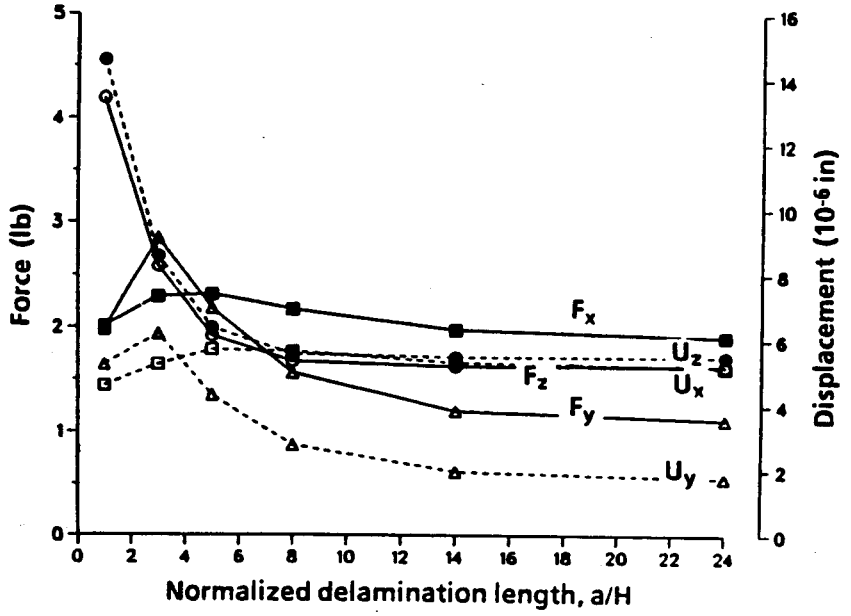

Figure 17. Forces and displacements used in calculation of strain energy release rates for $[90_4/0/\pm45]_S$ IM6/3501-6 graphite/epoxy laminate.

Effect of Hybrid Laminate

A family of quasi-isotropic laminates with a baseline of $[45/-45/0/90]_S$ and off-axis intervals of 15° was examined. The total strain energy release rate and the G_I, G_{II}, and G_{III} components were evaluated at three interfaces. For three of these laminates, the 90° graphite ply was replaced with a glass ply of S2/CE9000, creating a hybrid laminate; these laminates were $[45/-45/0/90]_S$, $[0/90/-45/45]_S$, and $[-45/45/90/0]_S$. As can be observed in Figures 18 through 20, the hybrid laminate consistently demonstrated a reduction in the total strain energy release rate. It is also noted that the $[-45/45/90/0]_S$ layup (Figure 20) has the highest strain energy release rate of the three layups. Moreover, at the 0/90 interface of this layup, the hybrid laminates exhibit a significant reduction in the Mode I strain energy release rate, G_I. Since G_I is considered to be a major contributor to static delamination, hybridization of soft 90°-ply laminates can significantly increase the delamination strength. Figures 21 through 24 depict the strain energy release rate components for the rest of the off-axis quasi-isotropic family. Of these, the [-45/45/90/0] layup has the highest G_I at the 45/90 interface.

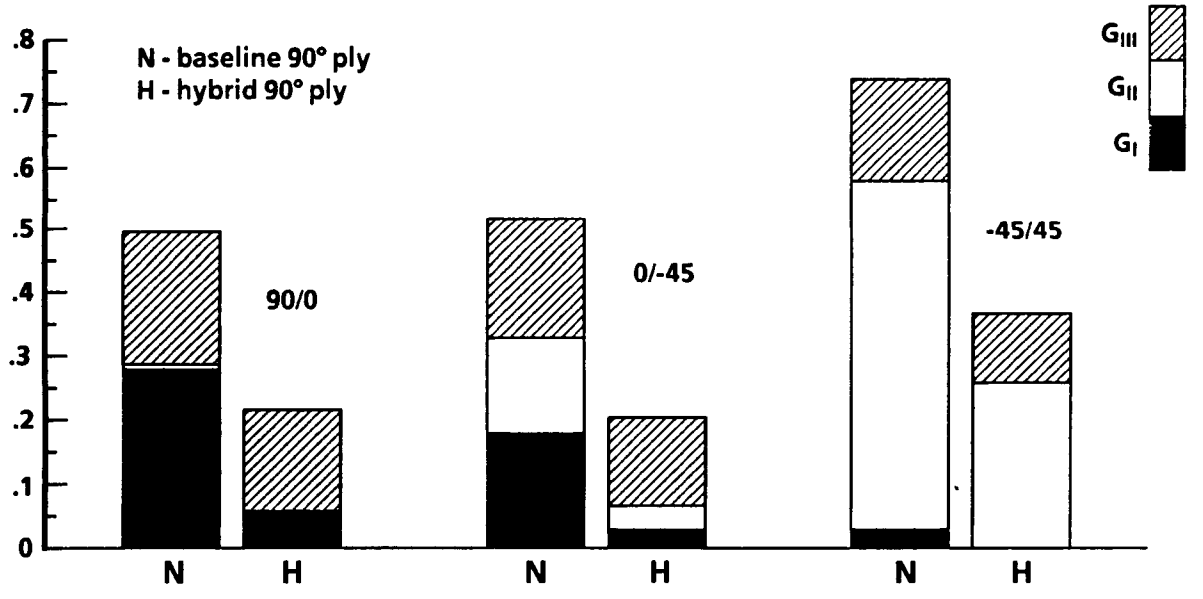

Figure 18. Comparison of strain energy release rates at various interfaces for the $[\pm 45/0/90]_S$ laminates, with and without the hybridizing 90° ply.

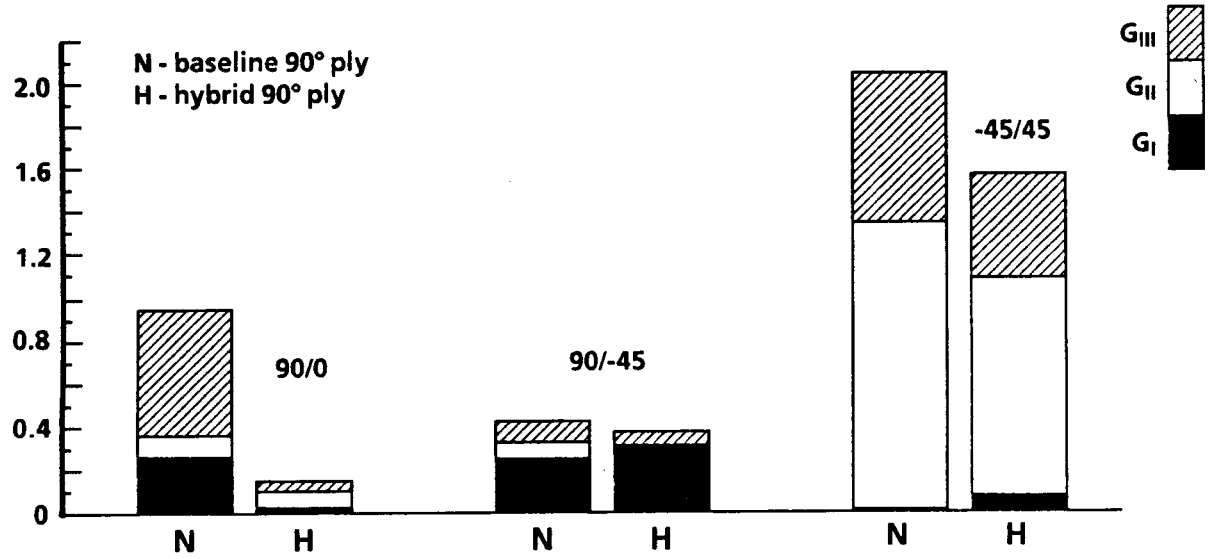

Figure 19. Comparison of strain energy release rates at various interfaces for the $[0/90/\mp 45]_S$ laminates, with and without the hybridizing 90° ply.

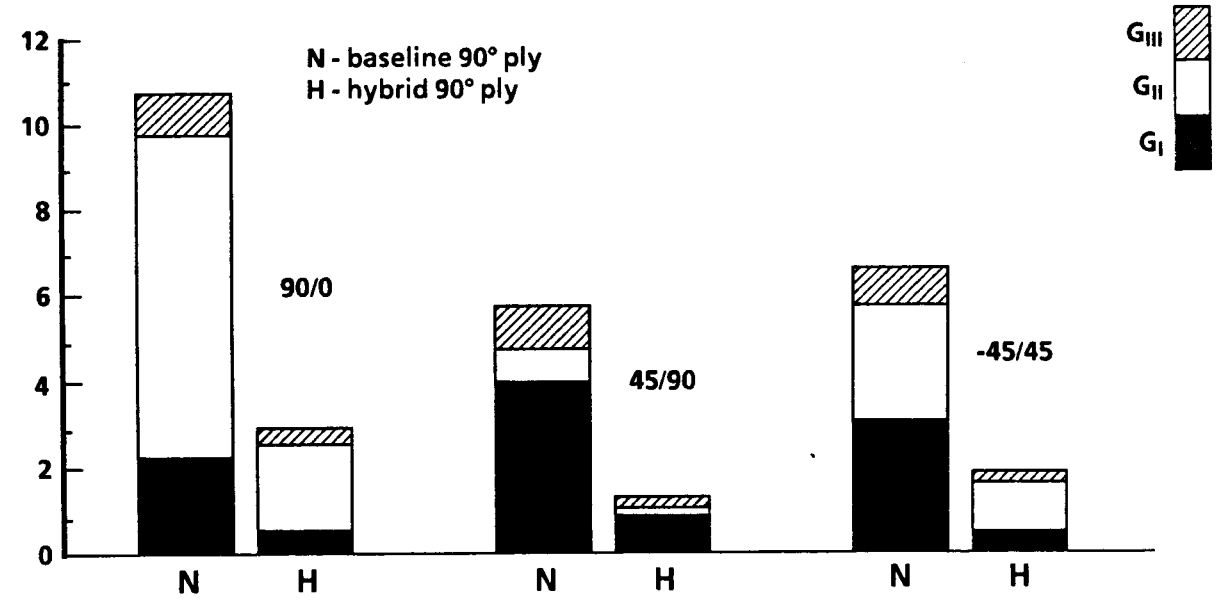

Figure 20. Comparison of strain energy release rates at various interfaces for the $[\mp 45/90/0]_S$ laminates, with and without the hybridizing 90° ply.

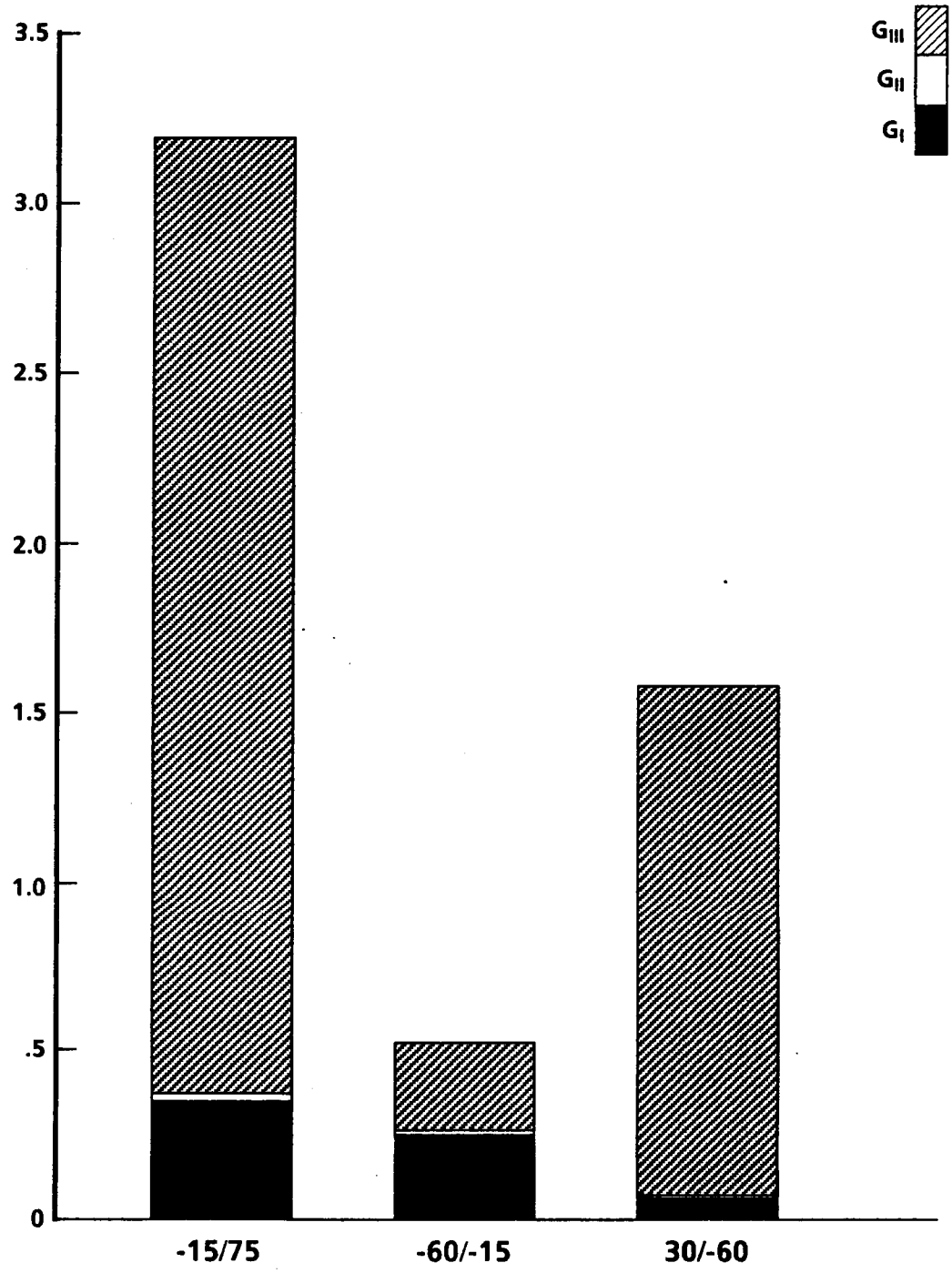

Figure 21. Variation of strain energy release rates at various interfaces for the $[30/-60/-15/75]_S$ laminates.

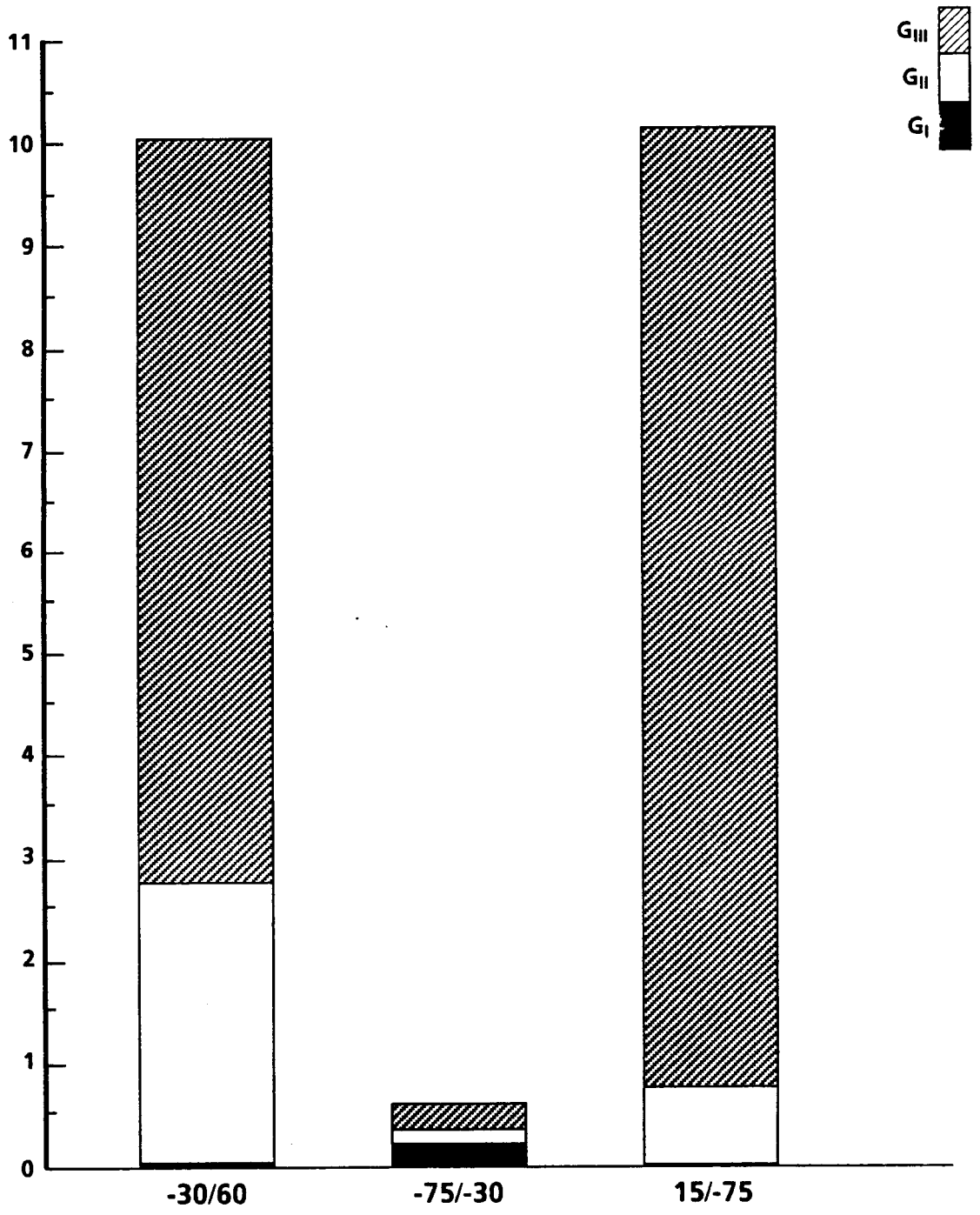

Figure 22. Variation of strain energy release rates at various interfaces for the $[15/-75/-30/60]_S$ laminates.

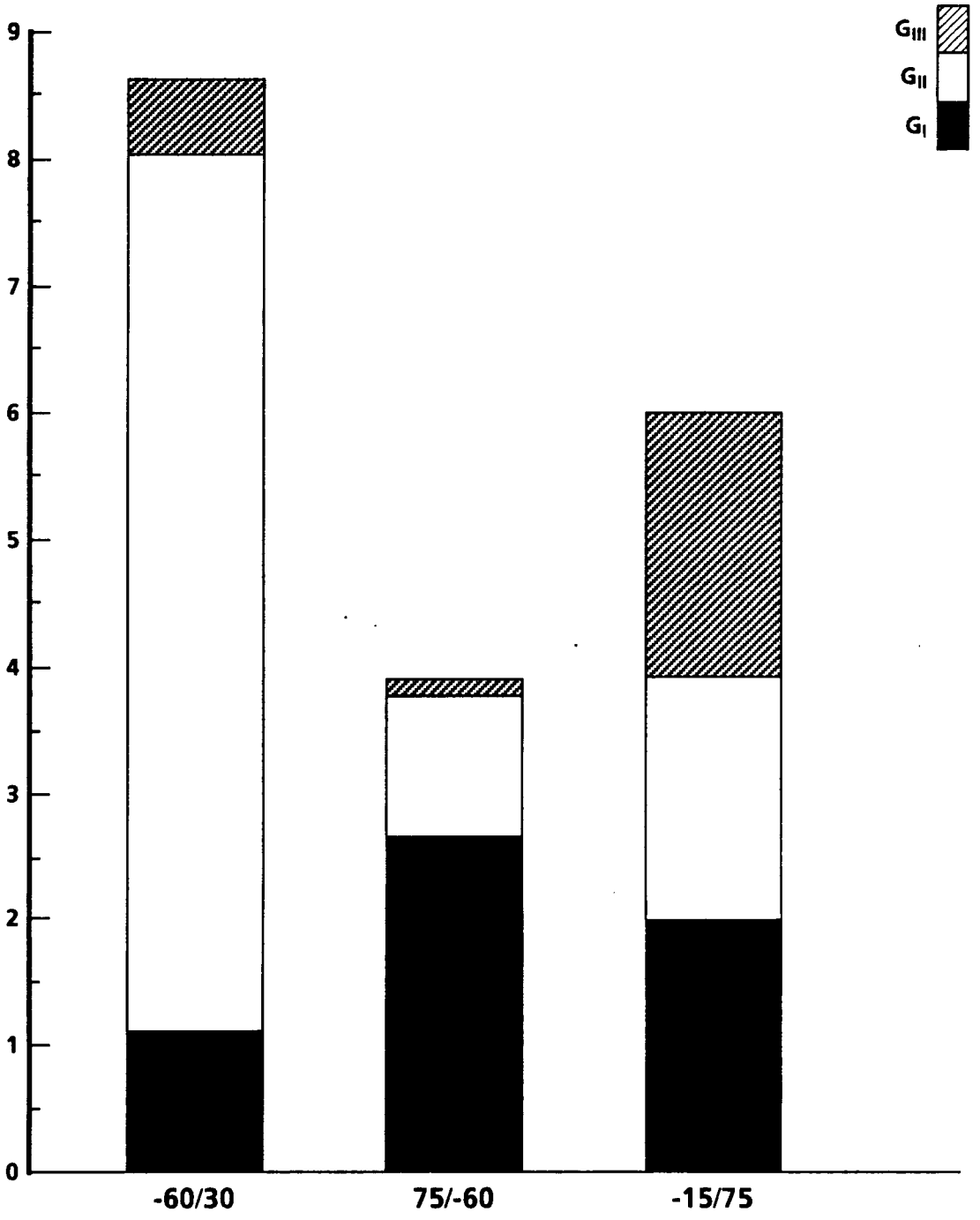

Figure 23. Variation of strain energy release rates at various interfaces for the $[-15/75/-60/30]_S$ laminates.

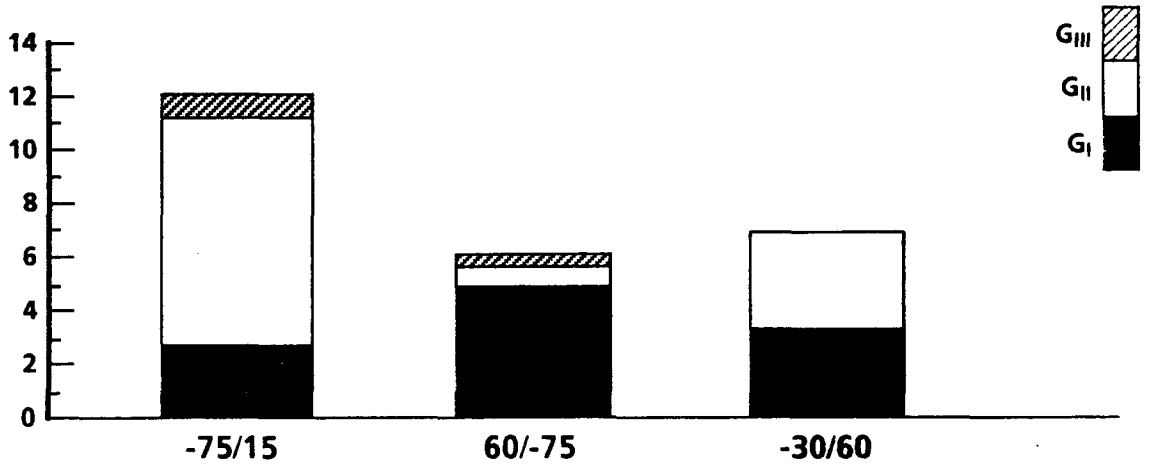

Figure 24. Variation of strain energy release rates at various interfaces for the $[-30/60/-75/15]_S$ laminates.

Preliminary Results on Torsion

Three layups of 16-ply IM6/3501-6 graphite/epoxy laminates - $[\pm 45]_{4S}$, $[\pm 45_2/0_2/90_2]_S$, and $[0]_{8S}$ - were studied under pure torsion loading. Two delaminations were assumed to be present, each extending in from the edge for a length equivalent to eight ply thicknesses. One was located at the top interface on one side of the laminate and the other was at the bottom interface on the opposite side. Their strain energy release rates for laminates subjected to a 0.1 twisting curvature are given in Table 6. As shown, a pure Mode III was achieved in the 0°-ply lamina, and the ±45 laminate yielded the highest G_T. The data also indicate that as the percentage of ±45 plies increases, G_{II}, G_{III}, and G_T increase. Further studies on delamination characteristics have also been performed by Chan and Ochoa (1987).

TABLE 6. STRAIN ENERGY RELEASE RATES FOR LAMINATES SUBJECTED TO A 0.1 TWISTING CURVATURE

G (in-lb/in^2)	$[\pm 45]_{4S}$	$[\pm 45_2/0_2/90_2]_S$	$[0]_{8S}$
G_I	0.1307	0.3332	0
G_{II}	1.0066	0.0181	0
G_{III}	1.9259	0.6872	0.2806
G_T	3.0632	1.0389	0.2806

EXPERIMENTS

The development of materials with delamination resistance has been of interest to both material manufacturers and designers for some time. While manufacturers have been devoted to improving toughness by altering the properties of the material, designers have focused on improving toughness by using conventional materials in innovative laminate constructions. New materials, such as toughened thermoset and thermoplastic matrices, have shown a significant increase in resistance to static delamination, but little improvement in resistance to fatigue (O'Brien, March 1987). On the other hand, innovative laminate constructions, using conventional materials and devices such as an inner layer (Chan et al., 1986), critical ply termination near the free edge (Chan and Ochoa, 1988), and a hybridized soft 90° ply, have exhibited a even greater improvement in static delamination resistance - far beyond the capability of the current toughened matrices. Both inner layer and critical ply termination concepts have also successfully demonstrated a remarkable increase in fatigue resistance. The hybrid laminates have not yet been tested for fatigue delamination resistance.

The purpose of this experimental program was to investigate the fatigue delamination characteristics of graphite/epoxy, glass/epoxy, and their hybrid laminates. The specific objectives were to establish the fatigue delamination thresholds for the Mode I and mixed-mode fatigue fractures of glass and graphite/glass hybrid laminates.

The static and fatigue thresholds for delamination were determined for both Mode I and mixed-mode fractures to characterize the material behavior of S2/SP250 glass/epoxy laminates. The fatigue characteristics of a hybrid laminate consisting of an AS4/3501-6 graphite/epoxy laminate with a 90° ply of S2/CE9000-9 glass/epoxy were investigated. Both 3501-6 and CE9000-9 matrix are 350°F cure resins.

STATIC AND FATIGUE TEST MATRIX

Edge delamination tension tests were first introduced by O'Brien (1980) to investigate the characteristics of delamination. Using layups such as $[\pm 30_2/90_3/\mp 30_2]_T$, O'Brien was able to measure delamination before final failure by reducing the amount of strain necessary to initiate the delamination. In this layup, the delamination grew at both the

top and bottom -30/90 interfaces, producing a mixed-mode fracture. Whitney and Knight (1985) modified this layup by embedding strips of a homogeneous material in the midplane of the laminate to force the delamination to grow at that plane, thus producing the Mode I fracture.

The test matrix and laminate layups, as well as the materials used in each test type, are outlined in Table 7. It should be noted that the hybrid coupons contain AS4/3501-6 graphite/epoxy plies for ±30° laminae and S2/CE9000-9 glass/epoxy plies for 90° laminae. A Tinius Olsen test machine was used for the static tests and an MTS 880 servohydraulic machine for the fatigue tests. The static tests were conducted to obtain the load at which static onset of delamination takes place, since this load is used in the determination of the maximum fatigue loads.

TABLE 7. COUPON TEST MATRIX

Test Type	Coupon Layup	Material	Load Type	Test	No. of Tests
Mode I	$[30/-30_2/30/90]_S$	S2/SP250	Static		2
			Fatigue	f = 1 Hz	9
			R=0.1	f = 5 Hz	9
Mixed-Mode	$[\pm 30_2/90_3/\mp 30_2]_T$	S2/SP250	Static		2
			Fatigue	f = 1 Hz	9
			R=0.1	f = 5 Hz	9
Mixed-Mode	$[\pm 30_2/90_{2GL}/\mp 30_2]_T$	AS4/3501-6	Static		2
	Hybrid	S2/CE9000-9	Fatigue	f = 1 Hz	9
			R=0.1	f = 5 Hz	9

COUPON PREPARATION AND GEOMETRY

Panels measuring 12 inches on each side were fabricated from each laminate. To simulate initial delaminations, 0.55-inch-wide strips of half-mil thick Kapton were placed in some panels. These strips were located 1 inch apart in the 0° direction

at the midplane of the laminate. Each panel was vacuum-bagged and autoclave-cured, with a final cure temperature of 250°F for glass laminates and 350°F for the graphite hybrid laminate, since SP250 is a 250°F curing matrix and both CE9000-9 and 3501-6 are 350°F curing matrices. The panels with the Kapton strips were cut along the centerline of each strip so that each coupon had a Kapton strip approximately 0.25 inch wide along its free edges. Before and after cutting, the panels and coupons were checked by C-scan for any imperfection that might have occurred during fabrication and cutting.

The coupon configurations for the laminates are shown in Figure 25. All coupons were approximately 1.5 inches wide and 10 inches long. Glass-laminate end tabs were attached to all coupons.

TEST PROCEDURE

Coupons with the Kapton-simulated initial delamination at both of the free edges were tested for Mode I fracture, while coupons without the Kapton were tested for mixed-mode fracture.

Static Tests

In the static tests, the coupon response during loading was monitored by means of a 1-inch MTS extensometer mounted on two V-notched aluminum plates attached to the test coupons 1 inch apart. An X-Y plotter was used to record the stress-strain behavior during loading. In the Mode I static test, two C-ring gages developed by Boeing Aircraft Corporation of Seattle were used to monitor the onset of delamination. In addition, a flashlight was shone through the back side of the coupons to enable visual detection of any delamination that might have occurred. In the mixed-mode test, checks for delamination were made by periodic visual inspections through a microscope. A typical coupon with the gages installed is shown in Figure 26.

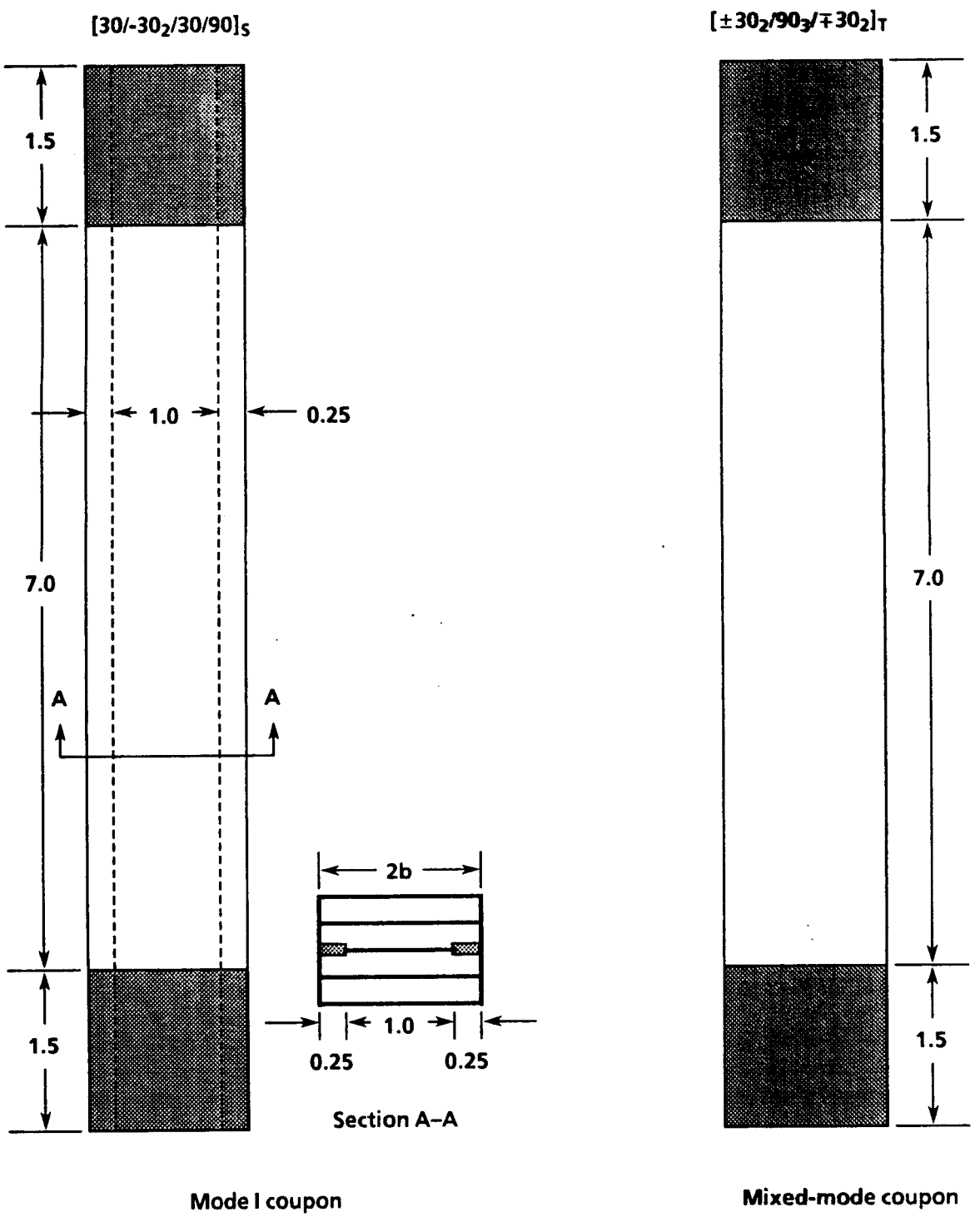

Figure 25. Coupon configurations for edge-delamination tension test.

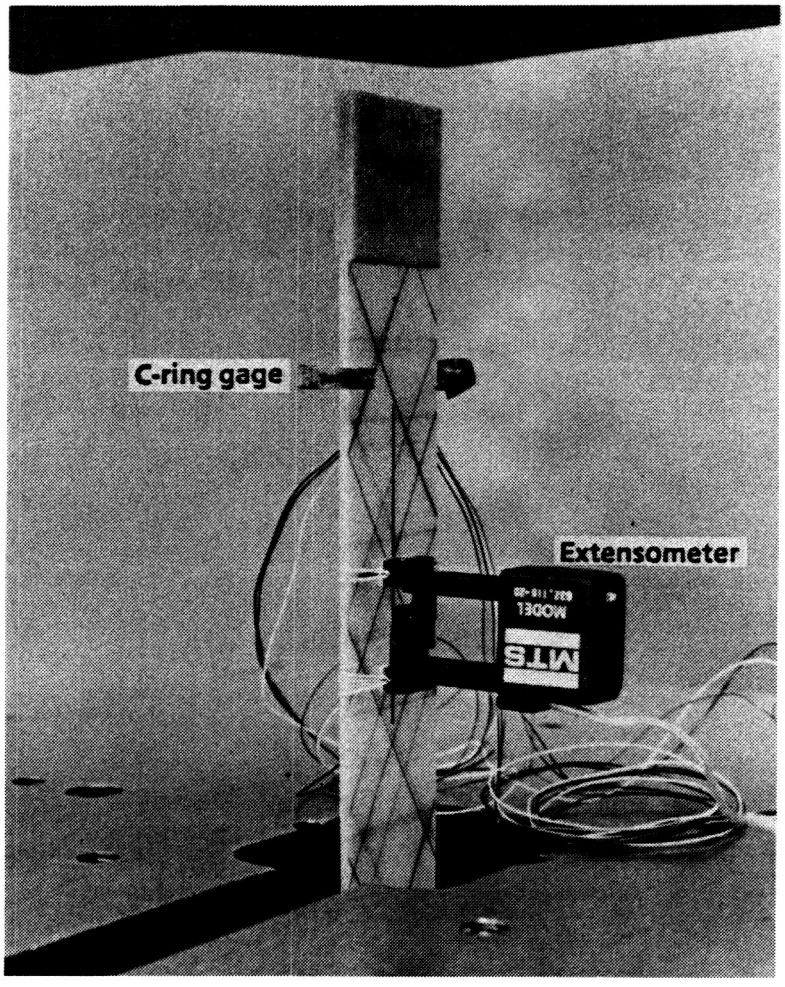

Figure 26. Setup for static tests.

Fatigue Tests

The fatigue tests were conducted at 1 and 5 Hz under maximum fatigue loads of 90%, 85%, 75%, and 60% of the static onset-of-delamination strength and a stress ratio of R ($=\sigma_{min}/\sigma_{max}$) = 0.1. The coupons were inspected for delamination growth at every 500 cycles from 0 to 5,000 cycles, at every 1000 cycles from 5,000 to 10,000 cycles, and at every 5,000 cycles from 10,000 to 100,000 cycles. If a delamination occurred, the inspection was conducted only at 5,000, 10,000, and 1,000,000 fatigue cycles. Dye penetrant was applied at the edge of the coupon to enhance detection of the delamination area. For glass/epoxy laminates, ink was used; for graphite/epoxy laminates, zinc iodide, which is opaque to x-rays, was used. Photographs were taken at the time of the inspection to document the delamination size. For graphite/epoxy

laminates, x-radiographs were taken. During all the tests, coupon edges were periodically checked by touch to see if any rise in temperature could be detected. Such a rise in temperature could indicate the release of energy and, hence, a change occurring within the coupon. Although subjective in nature, these tactile inspections are useful in initiating closer inspections of an objective nature.

TEST RESULTS AND DISCUSSION

The test results for each type will be discussed in the following section. The fracture toughness values (strain energy release rates) will also be presented.

Mode I Edge-Delamination Tension Test

Static Test Results

The static test results are listed in Table 8. The onset of delamination was measured from the stress-strain curve. Although the C-ring gage described in the previous section was mounted on the coupon to monitor the onset of delamination, there was some difficulty in measuring the onset value because of slippage of the gage. Therefore, the onset of delamination was measured at the change in slope on the stress-strain curve. A typical load-strain curve is plotted in Figure 27. The first slope change is caused by transverse cracks, and the subsequent slope change is caused by delamination. The measured value at the onset of delamination was verified by visual inspection (light shining through the back side of the coupon).

The unidirectional material constants listed in Table 9 were used to calculate the fracture toughness. The stress-free temperature used for estimating the thermal effect during curing was assumed to be 182°F. Subtracting the room temperature (72°F) results in a ΔT of -110°, which was the value used in calculating the Mode I fracture toughness (G_{IC}). The measured static onset-of-delamination strain and the calculated fracture toughness (see Appendix), with and without the thermal effects of curing, are included in Table 8. The results indicate that G_{IC} is significantly affected by the curing process. The initial delamination (Kapton) located at the midplane of the coupon divides

TABLE 8. STATIC G_{IC} FOR S2/SP250 GLASS/EPOXY

Coupon	UltimateStrength (ksi)	Measured Onset of Delamination		Calculated Interlaminar Fracture Toughness (in-lb/in^2)	
		Strength (ksi)	Strain (με)	With Thermal Effects	Without Thermal Effects
1	45.23	18.79	6300	0.630	0.286
2	45.07	17.33	6000	0.587	0.260
3	41.00	16.01	5700	0.545	0.234
Avg	43.77	17.38	6000	0.587	0.260

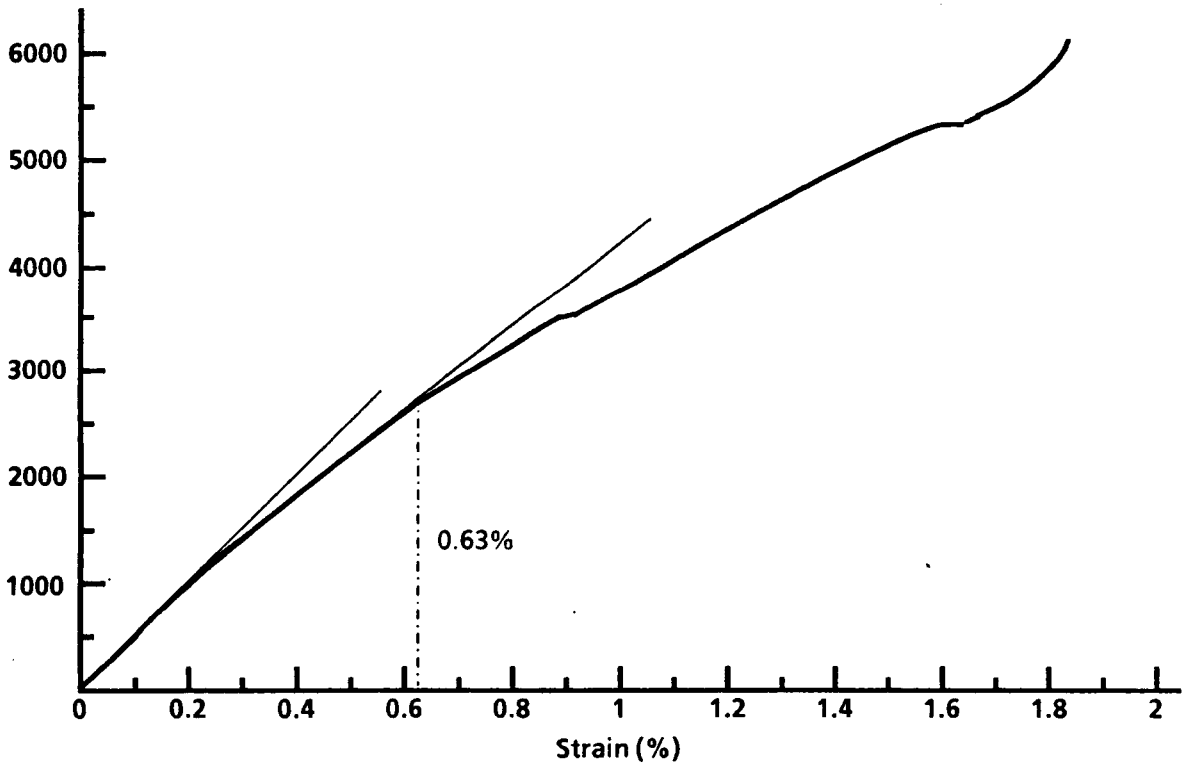

Figure 27. Typical load-strain curve for Mode I edge-delamination coupon.

TABLE 9. UNIAXIAL MATERIAL PROPERTIES FOR S2/SP250 GLASS/EPOXY LAMINATE

Material	E_1 (Msi)	E_2 (Msi)	G_{12} (Msi)	V_{12}	α_1 (με/°F)	α_2 (με/°F)	t_{ply} (in)
S2/SP250	6.31	2.50	0.60	0.25	10.73	42.12	0.0095
S2/CE9000-9	8.09	2.28	1.06	0.288	-	-	0.0074
AS4/3501-6	19.3	1.62	1.02	0.288	5	25	0.0052

the symmetric laminate into two unsymmetric sublaminates in the delamination region. Hence, the curing effect will play an important role in this type of test.

Fatigue Test Results

Figures 28, 29, and 30 show delamination growth, Δa, beyond the initial delamination (Kapton strip) for coupons subjected to 90%, 85%, and 75% of the static onset-of-delamination load, respectively. The delamination growth, Δa, was measured from the maximum extent at the same six selected locations for all the coupons. The selected locations were located approximately at the middle length of the coupon, and 2 inches up and down from the middle length on each side of the coupon. This procedure was then used for all the coupons tested in this study. The growth is plotted as a function of number of fatigue cycles and has been normalized by coupon width, b. The delamination growth was measured during the inspection intervals. The figures also show data from the two vibration rates used, 1 Hz and 5 Hz. Although the indication is not strong, there appears to be a tendency, under all three loads, for the delamination to grow faster at 1 Hz than at 5 Hz.

The fatigue delamination onset was selected as that point at which the delamination growth beyond the initial length reached 3% of the coupon width. This value was determined by a least-squares curve fit of the data shown in Figures 28, 29, and 30. The delamination growth shown in these figures is the growth beyond the width of the Kapton strip. Table 10 shows the resulting fatigue delamination onset for the Mode I coupons. In Figure 31, these values are plotted against the applied load, which is given as a fraction (or percentage) of the static onset-of-delamination, σ/σ_o. A straight line, least-squares fitted on a semi-logarithmic scale, is drawn through the data and extrapolated to 1×10^6 cycles, which was assumed to be the endurance life. To achieve this, the load, σ/σ_o, for Mode I would be approximately 0.60.

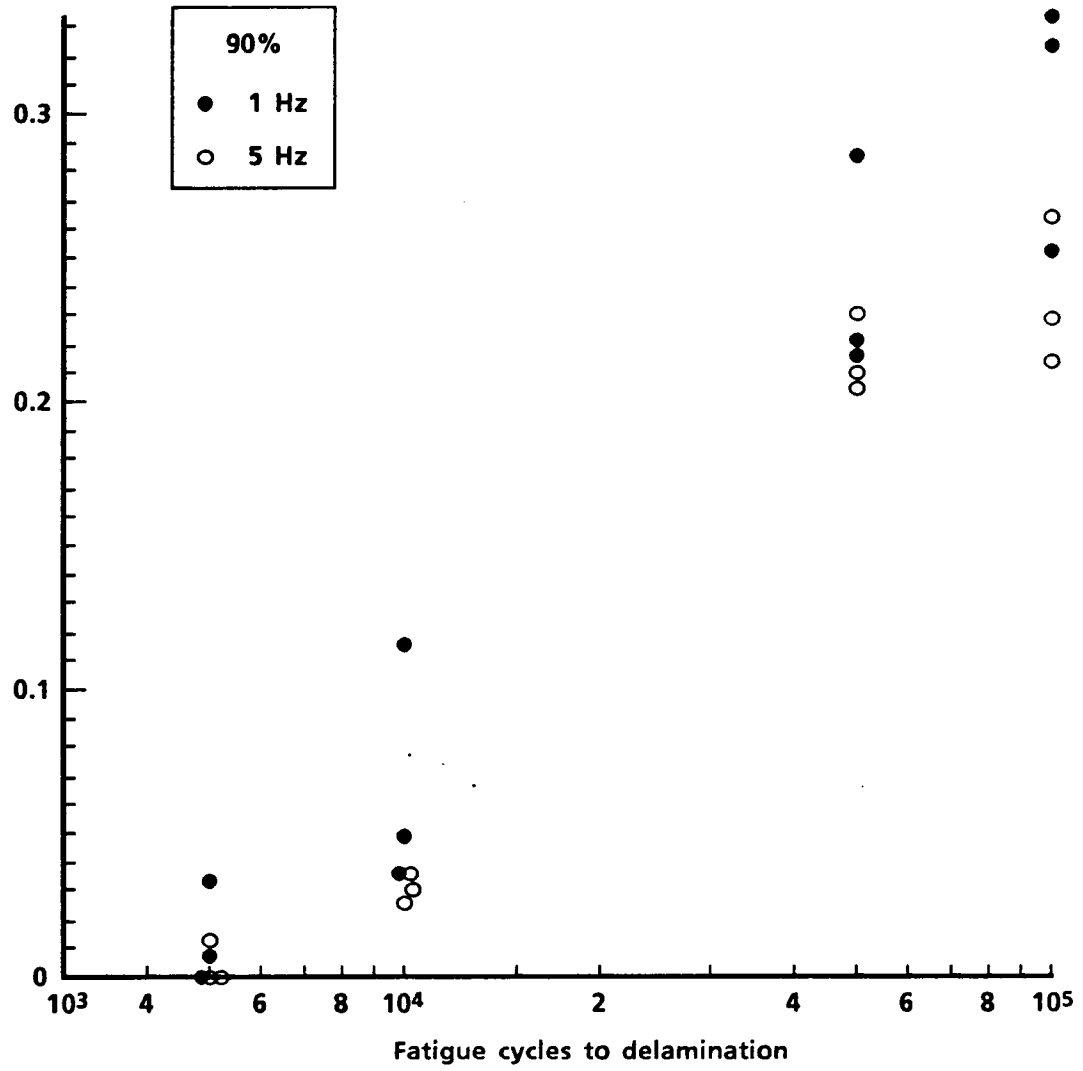

Figure 28. Delamination growth in Mode I coupons during fatigue testing with $\sigma_{max} = 0.90\,\sigma_o$.

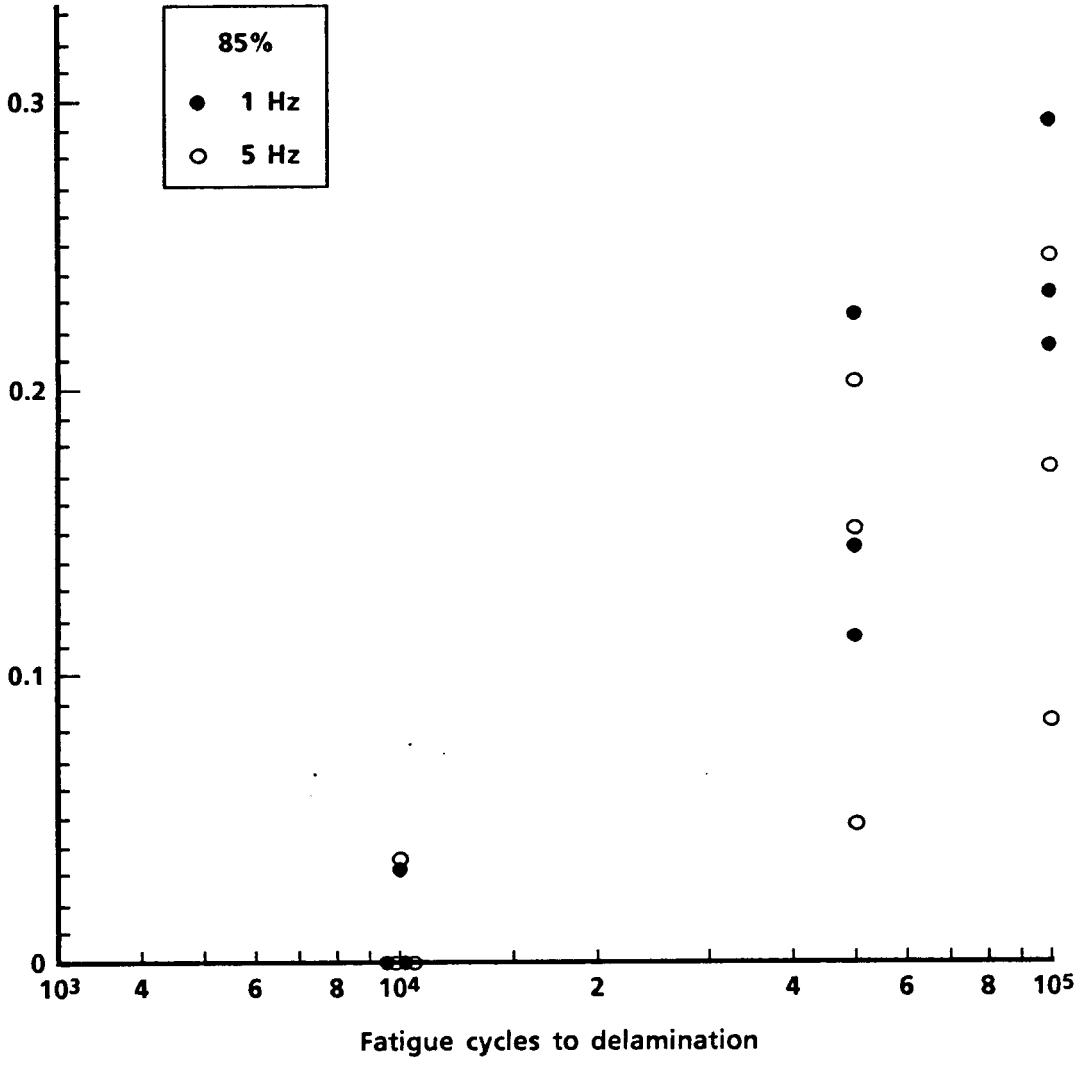

Figure 29. Delamination growth in Mode I coupons during fatigue testing with $\sigma_{max} = 0.85\,\sigma_o$.

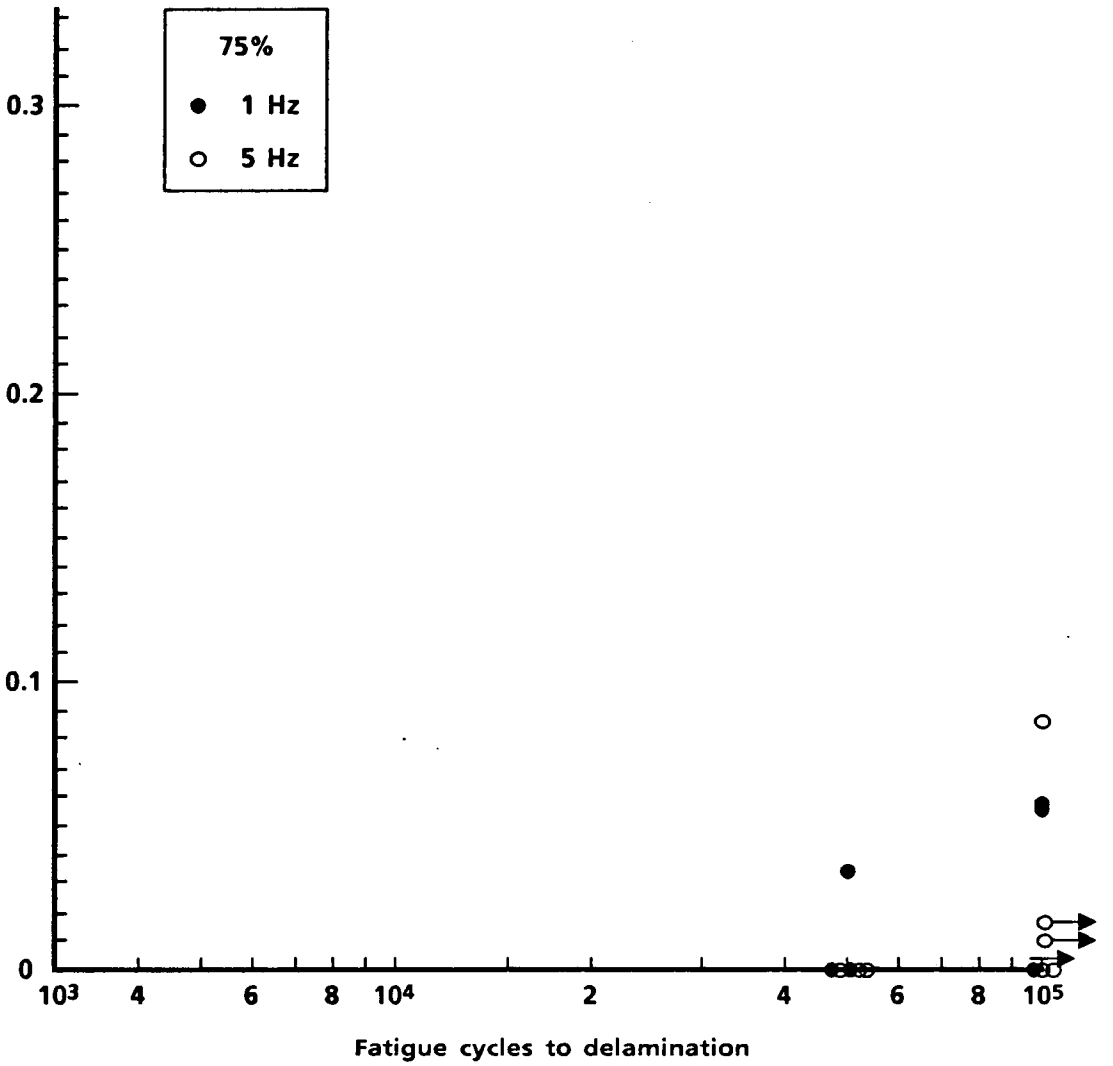

Figure 30. Delamination growth in Mode I coupons during fatigue testing with $\sigma_{max} = 0.75\,\sigma_o$.

TABLE 10. FATIGUE DELAMINATION ONSET FOR MODE I EDGE-DELAMINATION GLASS/EPOXY COUPONS

Coupon	Width × Thickness (in × in)	[a] σ/σ_0	Freq (Hz)	Fatigue Delamination Onset (cycles)	Avg (cycles)
1	1.507 × 0.098	0.90	1	8,793	
2	1.502 × 0.096	0.90	1	7,338	6,871
3	1.507 × 0.100	0.90	1	4,483	
4	1.494 × 0.099	0.90	5	8,702	
5	1.493 × 0.097	0.90	5	10,240	8,791
6	1.496 × 0.096	0.90	5	7,432	
7	1.494 × 0.098	0.85	1	15,860	
8	1.495 × 0.100	0.85	1	9,671	15,067
9	1.504 × 0.100	0.85	1	19,670	
10	1.503 × 0.098	0.85	5	34,580	
11	1.491 × 0.099	0.85	5	9,047	19,082
12	1.500 × 0.098	0.85	5	13,620	
13	1.496 × 0.101	0.75	1	72,390	
14	1.501 × 0.098	0.75	1	45,530	>72,640
15	1.505 × 0.099	0.75	1	$>1 \times 10^5$	
16	1.500 × 0.100	0.75	5	$>1 \times 10^5$	
17	1.500 × 0.100	0.75	5	63,550	>87,850
18	1.502 × 0.101	0.75	5	$>1 \times 10^5$	

[a] σ/σ_0 = Maximum fatigue load/static onset of delamination; static delamination strength = 17.38 ksi

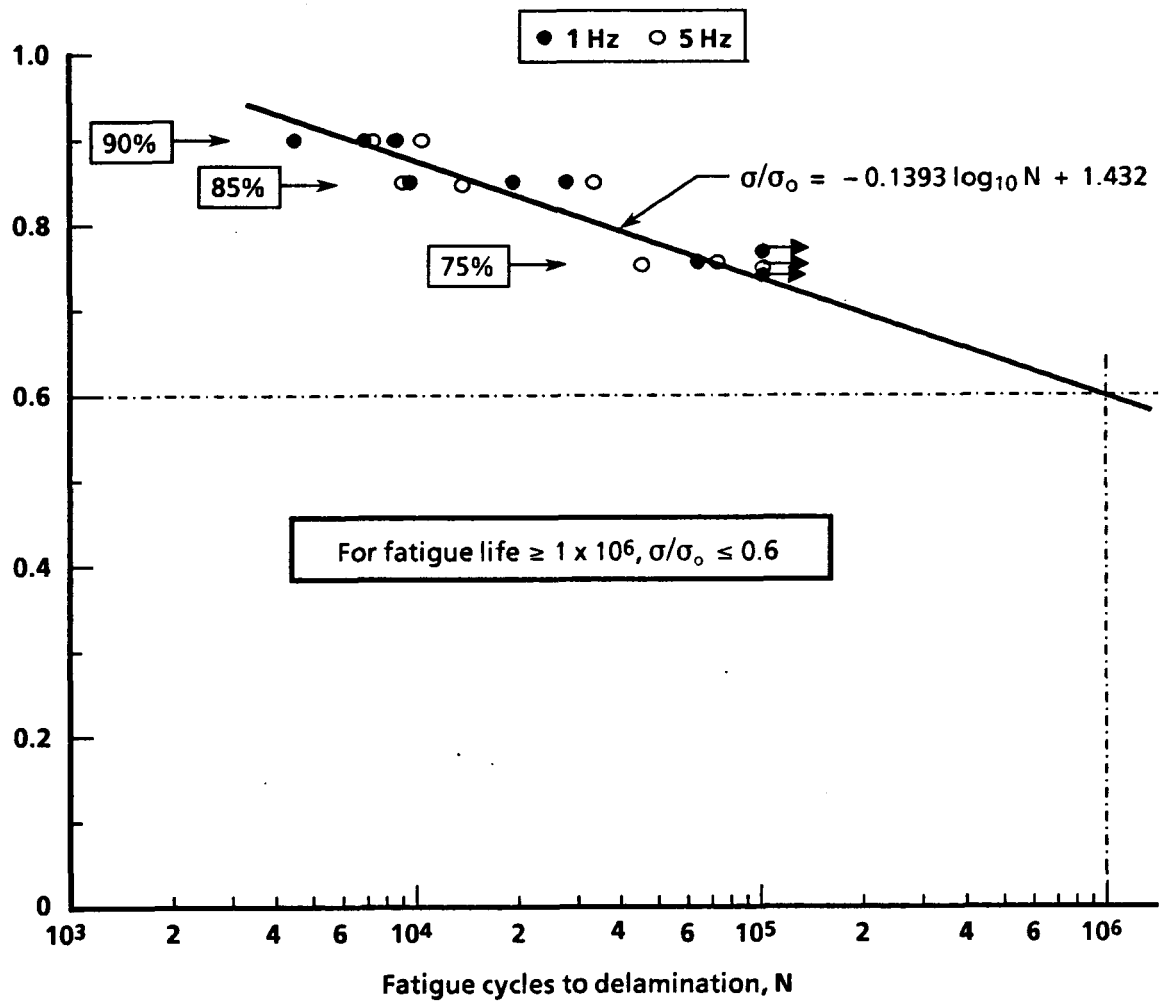

Figure 31. Effect of load level on fatigue life of Mode I edge-delamination glass/epoxy coupons.

Mixed-Mode Edge-Delamination Test for Glass/Epoxy Coupons

Static Test Results

Table 11 lists the static test results for the glass/epoxy mixed-mode coupons. The onset-of-delamination strength shown in the table will serve as a guide in determining the fatigue load. The values for interlaminar fracture toughness, G_c, were calculated by the following equation:

$$G_c = \frac{\varepsilon_c^2 t}{2}\left(E_{lam} - E^*\right)$$

where ε_c = axial strain at the onset of delamination

t = laminate thickness

E_{lam} = laminate axial stiffness calculated from laminated plate theory

E^* = axial stiffness of a fully delaminated laminate

For the $[\pm 30_2/90_3/\mp 30_2]_T$ laminate, delamination occurred at the interface between the -30° and 90° plies. E^* was calculated as follows:

$$E^* = \frac{8E_{(\pm 30)s} + 3E_{90}}{11}$$

A detailed discussion of the above method can be found in O'Brien et al. (1982) and *Standard Tests for Toughened Resin Composites* (1983).

TABLE 11. STATIC TEST RESULTS FOR MIXED-MODE EDGE-DELAMINATION COUPONS

Coupon	Onset of Delamination Strength (ksi)	Onset of Delamination Strain (με)	Interlaminar Fracture Toughness, G_c (in-lb/in^2)
1	21.28	7600	0.818
2	21.55	7300	0.754
Avg	21.42	7450	0.786

Fatigue Test Results

As described in the Mode I test, the fatigue delamination onset was determined at the life when the delamination reached 3% of the lamination width. Table 12 presents the fatigue delamination onset for the S2/SP250 glass/epoxy coupons subjected to mixed-mode fracture. In Figure 32, the fatigue delamination onset values are plotted against the applied load, σ/σ_0, and a least-squares-fitted straight line drawn through the data and extrapolated to 1 x 10^6 cycles. This shows that for a delamination life greater than 10^6 cycles, the maximum fatigue load cannot be above 43% of the static onset-of-delamination strength. Figure 33 shows, for comparison, one of the coupons after 5,000 cycles and again after 100,000 cycles.

Mixed-Mode Edge-Delamination Test for Hybrid Coupons

In this section, the results of static and fatigue tests on both graphite and graphite/glass hybrid coupons are reported. The all-graphite/epoxy results generated under a Bell IR&D program serve as a baseline for comparison with the hybrid coupon results.

Static Test Results

Table 13 summarizes the static test results of coupons with and without a glass hybridization. The data indicate a 20% increase in delamination strength and a 10% increase in ultimate strength for the hybrid laminate compared to the baseline. This improvement was observed by Chan and Wang in 1986. The improvement in delamination strength can be explained by the reduction in strain energy release rate shown by the analysis. For both the baseline and hybrid laminates, delamination was observed as wandering at the interfaces between the -30° and 90° layers and between the 90° layers.

Fatigue Test Results

Tables 14 and 15 summarize the fatigue test results for the graphite and graphite/glass hybrid coupons, respectively. It is evident that the hybrid coupons have

TABLE 12. FATIGUE DELAMINATION ONSET FOR MIXED-MODE EDGE-DELAMINATION GLASS/EPOXY COUPONS

Coupon	Width × Thickness (in × in)	$^{a}\sigma/\sigma_0$	Freq (Hz)	Fatigue Delamination Onset (cycles)	Avg
2	1.486 × 0.105	0.90	1	500	
3	1.498 × 0.106	0.90	1	572	536
4	1.502 × 0.105	0.90	5	463	
5	1.495 × 0.106	0.90	5	303	
6	1.505 × 0.104	0.90	5	702	489
8	1.498 × 0.103	0.75	1	8,201	
9	1.481 × 0.105	0.75	1	5,469	6,840
10	1.500 × 0.104	0.75	5	4,579	
11	1.485 × 0.106	0.75	5	3,438	4,009
12	1.492 × 0.104	0.70	1	9,647	
13	1.499 × 0.104	0.70	1	8,993	9,320
14	1.498 × 0.104	0.70	5	10,680	
15	1.486 × 0.105	0.70	5	8,579	9,630
16	1.496 × 0.106	0.60	1	62,280	
17	1.496 × 0.105	0.60	1	80,220	71,250
18	1.486 × 0.105	0.60	5	56,780	56,780

$^{a}\sigma/\sigma_0$ = Maximum fatigue load/static onset of delamination; static delamination strength = 21.42 ksi

a lower threshold life than the baseline coupons. Figures 34 and 35 show the fatigue delamination onset plotted against appplied load, σ/σ_O, and a least-squares-fitted straight line drawn through the data and extrapolated to 1 x 10^6 cycles. For an endurance life greater than 10^6 cycles, the maximum fatigue load cannot exceed 59% of static onset-of-delamination strength for the baseline coupon and 51% of same delamination strength for the hybrid laminate. It is concluded that although the hybrid laminate can improve both the static delamination and ultimate strength, it lowers the fatigue delamination onset

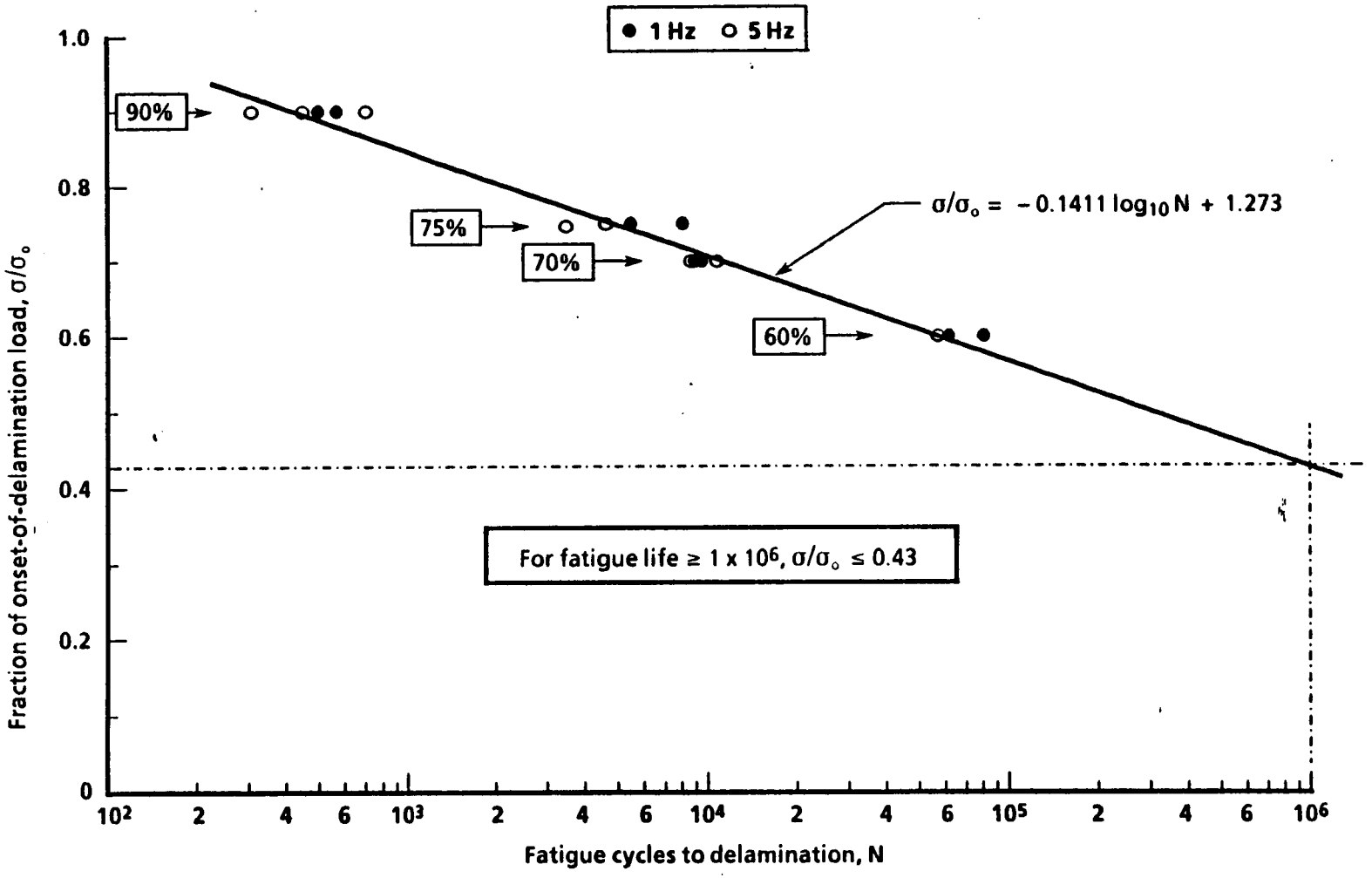

Figure 32. Effect of load level on fatigue life of mixed-mode edge-delamination glass/epoxy coupons.

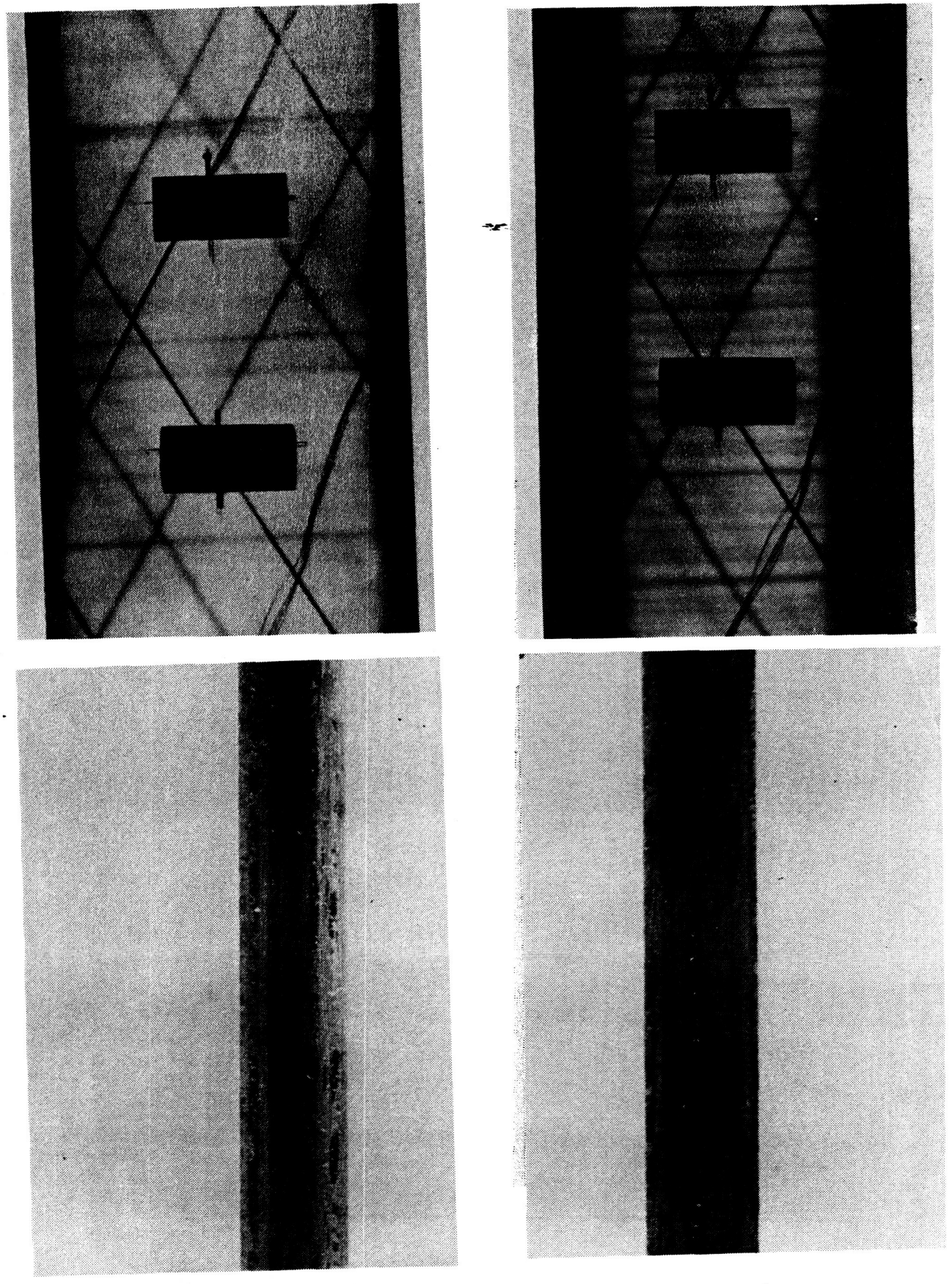

After 5,000 cycles

After 100,000 cycles

Figure 33. Mixed-mode edge-delamination glass/epoxy coupon after 5,000 and 100,000 cycles.

TABLE 13. MIXED-MODE DELAMINATION TENSION TEST FOR GRAPHITE/ EPOXY WITH AND WITHOUT A GLASS HYBRIDIZATION

Coupons	Dimension Width × Thickness (in × in)	Onset of Delamination Strength (ksi)	Onset of Delamination Strain (με)	Ultimate Strength (ksi)
All-graphite	1.498 × 0.061	26.05	3800	64.25
	1.493 × 0.059	30.08	3900	63.57
Avg		28.07	3850	63.91
Hybrid	1.503 × 0.060	33.05	5200	68.93
	1.502 × 0.061	34.11	4840	71.16
Avg		33.58	5020	70.05

TABLE 14. FATIGUE DELAMINATION ONSET FOR BASELINE EDGE-DELAMINATION GRAPHITE COUPONS

Coupon	Width × Thickness (in × in)	$\frac{\sigma}{\sigma_0}$[a]	Freq (Hz)	Fatigue Delamination Onset (cycles)	Avg
1	1.494 × 0.058	0.90	1	276	276
2	1.492 × 0.058	0.90	5	78	78
3	1.493 × 0.059	0.75	1	7,458	
4	1.495 × 0.058	0.75	1	4,480	5,969
5	1.492 × 0.060	0.75	5	27,140	
6	1.494 × 0.058	0.75	5	17,810	22,475
7	1.493 × 0.061	0.70	1	23,050	
8	1.493 × 0.060	0.70	1	$>1 \times 10^5$	>61,525
9	1.495 × 0.059	0.70	5	23,640	
10	1.493 × 0.063	0.70	5	$>1 \times 10^5$	>61,820
11	1.492 × 0.062	0.60	1	$>1 \times 10^5$	>100,000
12	1.493 × 0.063	0.60	5	$>1 \times 10^5$	>100,000

[a] σ/σ_0 = Maximum fatigue load/static onset of delamination; static delamination strength = 28.07 ksi

TABLE 15. FATIGUE DELAMINATION ONSET FOR HYBRID EDGE-DELAMINATION GRAPHITE/GLASS COUPONS

Coupon	Width × Thickness (in × in)	$\frac{^a\sigma}{\sigma_0}$	Freq (Hz)	Fatigue Delamination Threshold (cycles)	Avg
1	1.499 × 0.061	0.90	1	102	102
2	1.500 × 0.060	0.90	5	93	93
3	1.495 × 0.060	0.75	1	4,058	
4	1.498 × 0.064	0.75	1	2,620	3,190
5	1.500 × 0.060	0.75	1	2,892	
6	1.499 × 0.060	0.75	5	3,570	
7	1.497 × 0.060	0.75	5	2,261	3,291
8	1.500 × 0.059	0.75	5	4,041	
9	1.500 × 0.062	0.70	1	3,693	
10	1.499 × 0.060	0.70	1	11,770	10,208
11	1.499 × 0.059	0.70	1	15,160	
12	1.498 × 0.060	0.70	5	14,770	
13	1.501 × 0.060	0.70	5	18,790	14,657
14	1.501 × 0.060	0.70	5	10,410	
15	1.501 × 0.059	0.60	1	24,640	
16	1.501 × 0.060	0.60	1	38,580	31,610
17	1.501 × 0.060	0.60	5	243,400	
18	1.494 × 0.064	0.60	5	>100,000	>100,000

[a] σ/σ_0 = Maximum fatigue load/static onset of delamination; static delamination strength for baseline laminate = 28.07

Figure 36 presents x-radiographs of two pairs of baseline and hybrid coupons after 100,000 cycles under a load of 90% on the static onset of delamination. One pair was subjected to a rate of 1 Hz, and the other pair to a rate of 5 Hz. As can be seen, there are no significant differences in the delamination growth at this load level.

In contrast to the coupons under 90% load, Figure 37 shows that delamination grows faster in the hybrid than in the baseline when a load level of 75% is applied at a rate of 1 Hz. The x-radiographs in this figure were also taken after 100,000 cycles.

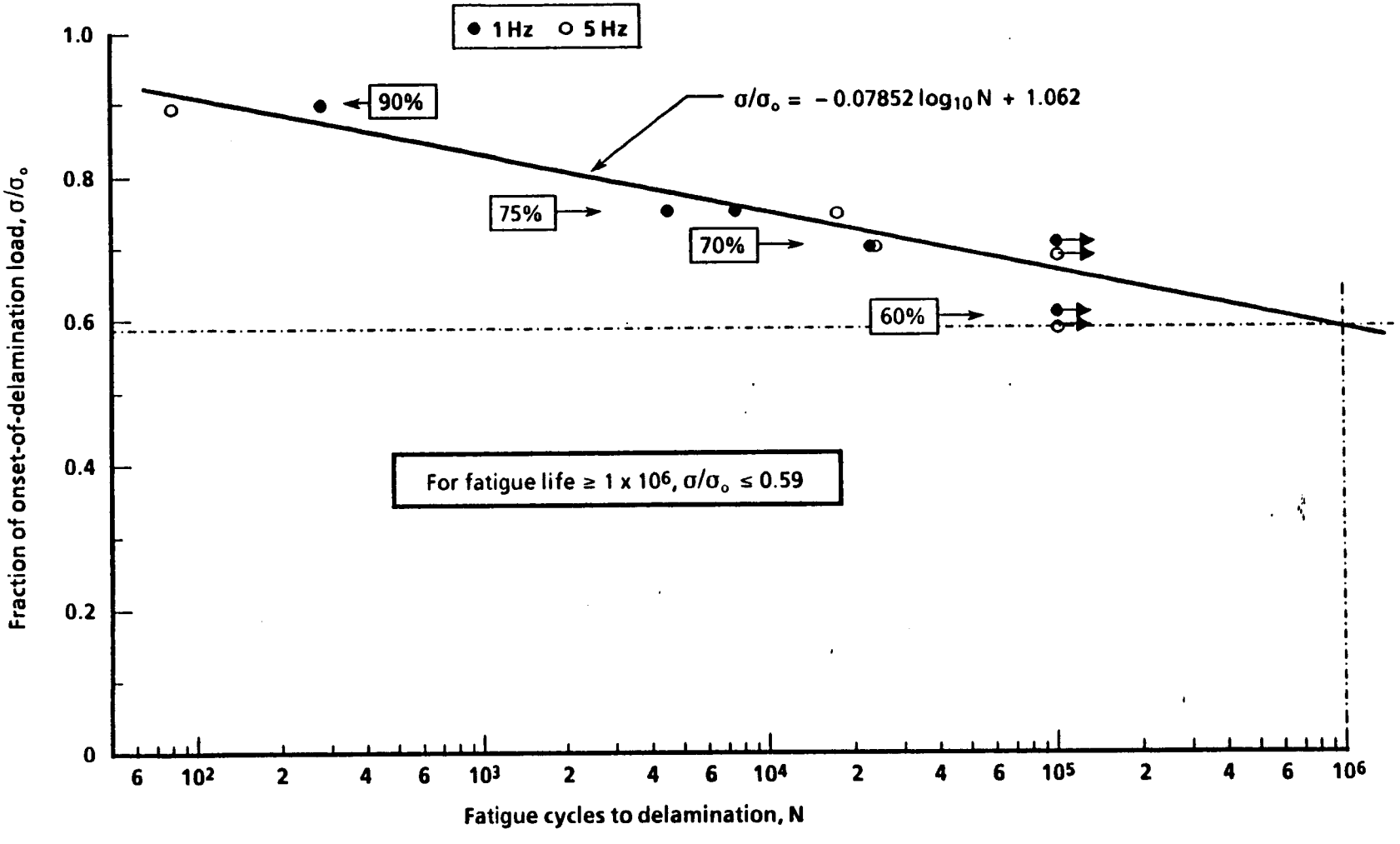

Figure 34. Effect of load level on fatigue life of mixed-mode edge-delamination graphite/epoxy coupons.

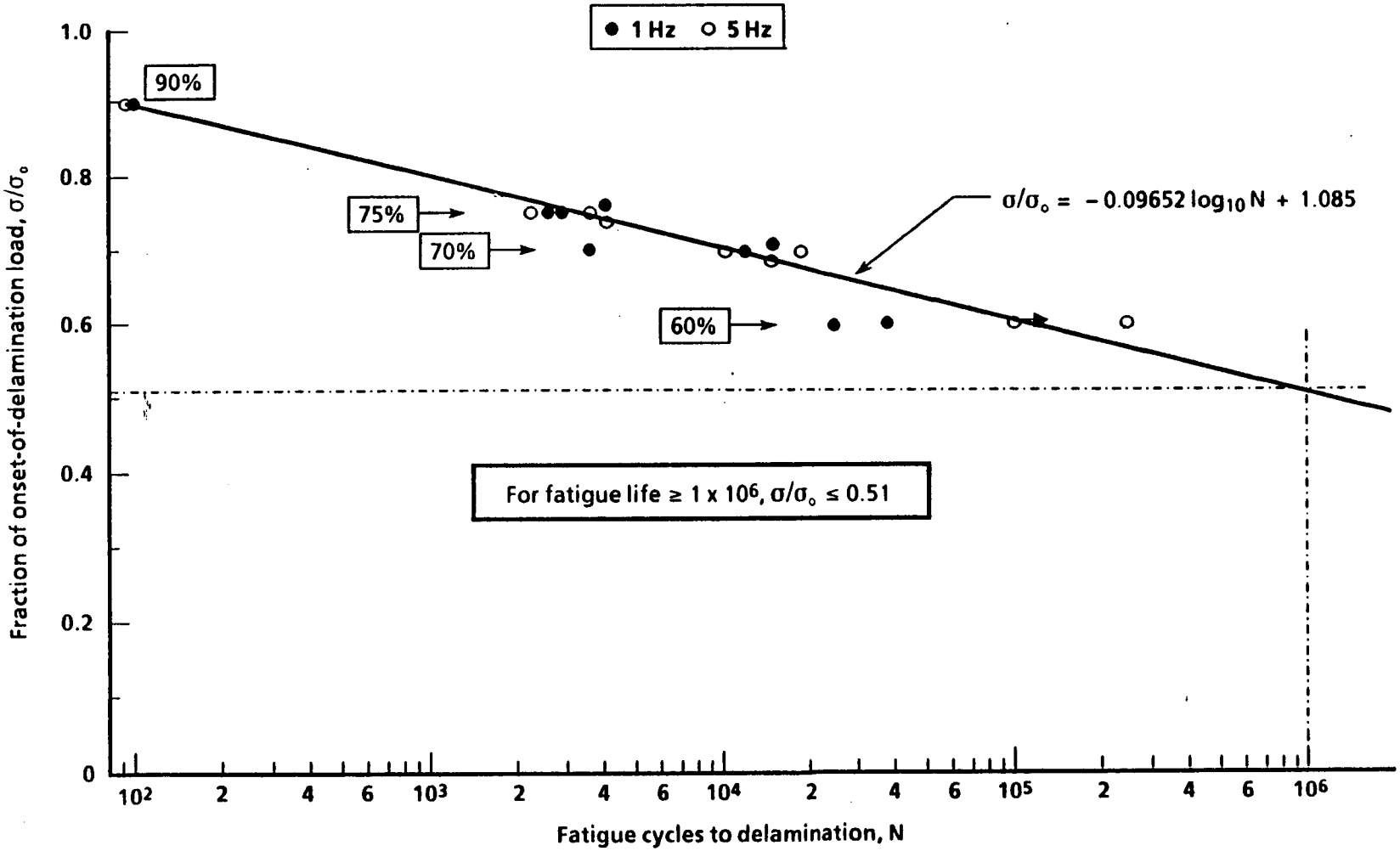

Figure 35. Effect of load level on fatigue life of mixed-mode edge-delamination graphite/glass hybrid coupons.

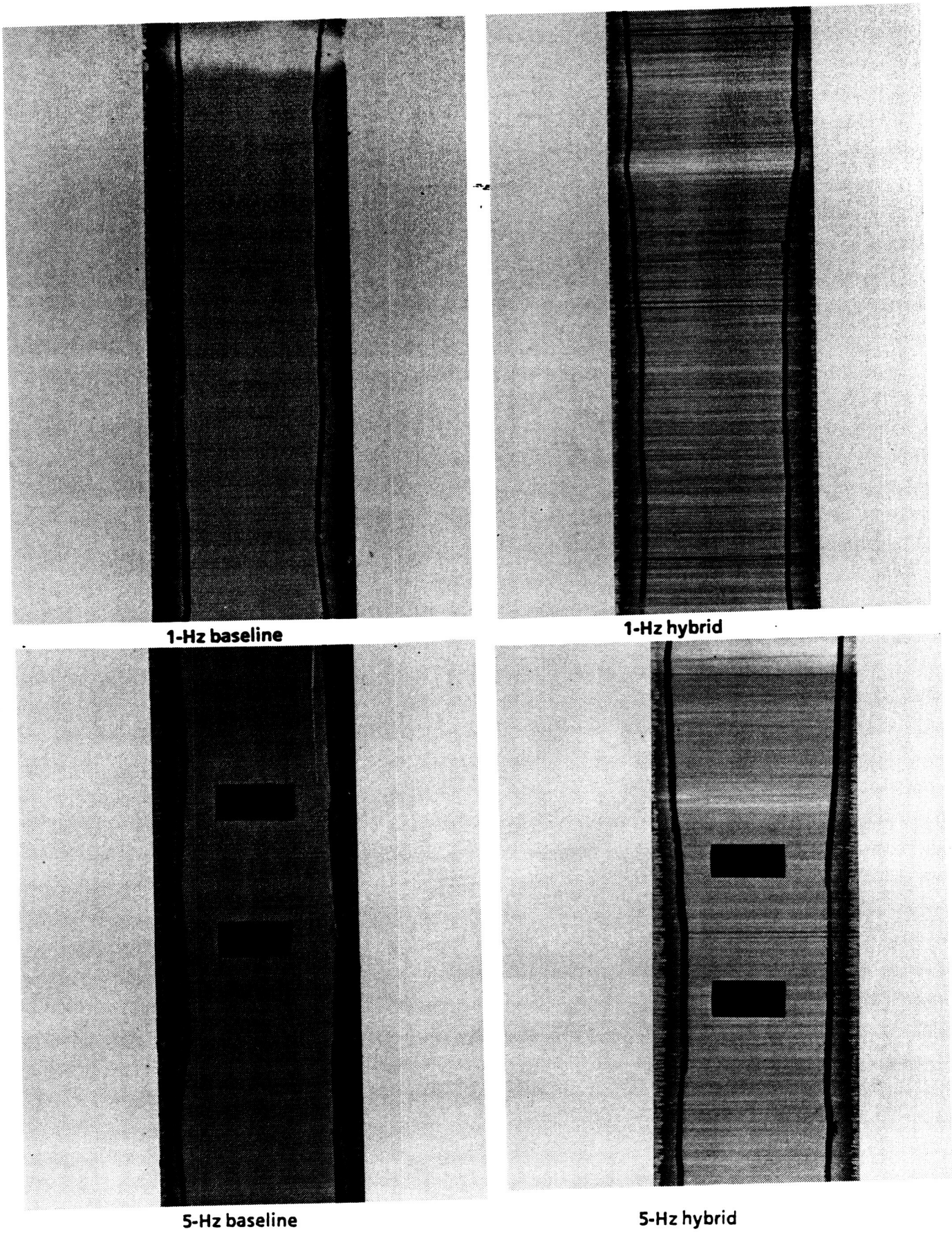

Figure 36. Comparison of 1- and 5-Hz baseline and hybrid graphite coupons after 100,000 cycles under 90% load.

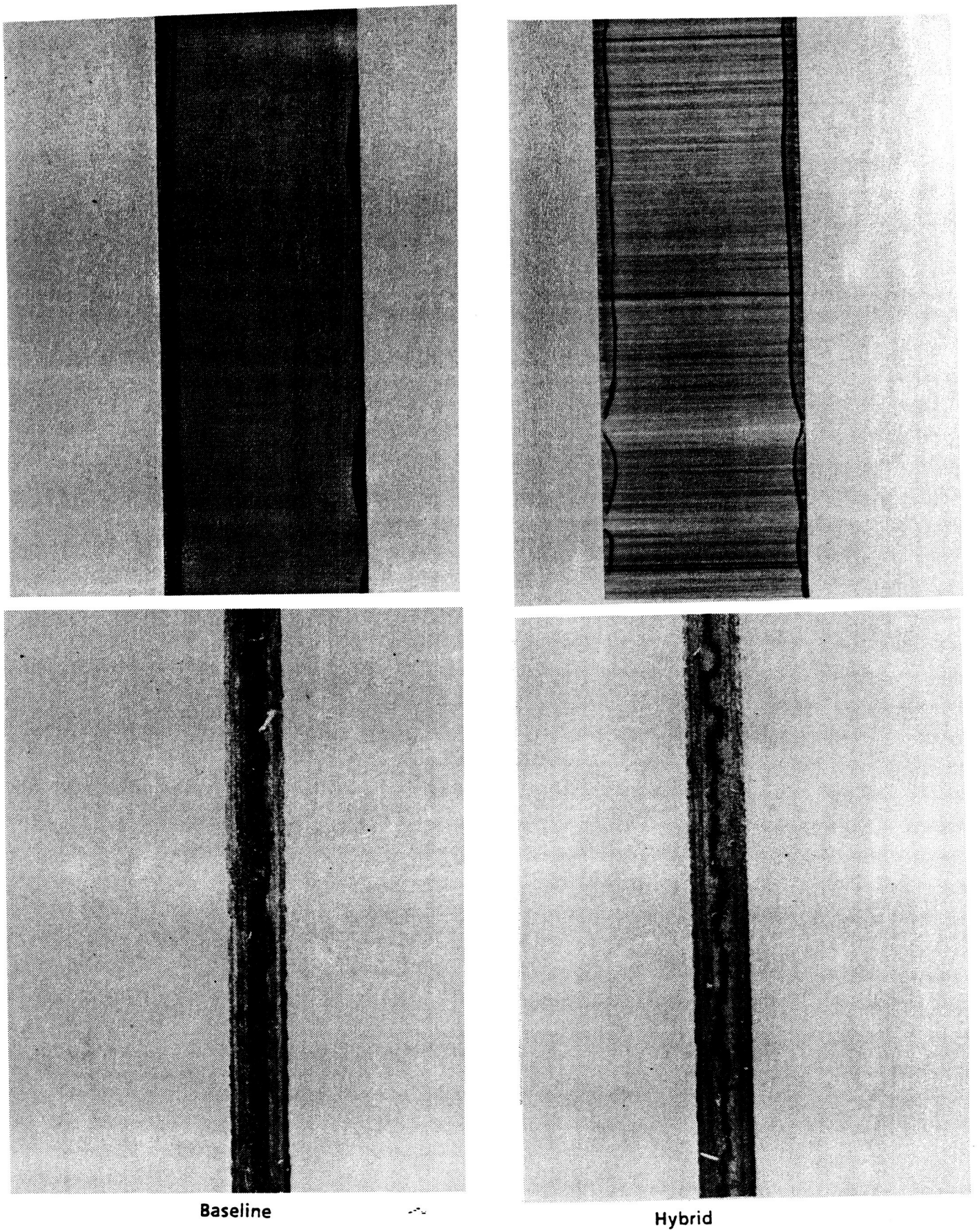

Figure 37. Comparison of 1-Hz baseline and hybrid graphite coupons after 100,000 cycles under 75% load.

CONCLUSIONS

A simple quasi-three-dimensional finite-element model has been developed and successfully used to study the free edge stress as well as the edge delamination characteristics of laminates subjected to uniaxial, bending, and torsional loads. This analysis and specimen tests of conventional as well as innovative layups have led to the following conclusions:

1. For a laminate under bending, minimizing the Poisson's ratio difference between plies or stacking the primary load-carrying plies far from the mid-plane can significantly reduce the interlaminar stresses and strain energy release rates.

2. Unlike the tension case, the total (G_T) and Mode I strain energy release rates for laminates under bending decrease as delamination length increases and reaches a lower bound.

3. G_{II} and G_{III}, as well as G_T, increase as the percentage of 45° plies increases for a laminate subjected to torsion.

4. The static onset-of-delamination strength and strain, as well as the ultimate strength, are higher in the graphite/epoxy laminates with the hybridized 90° glass ply than in the baseline all-graphite laminates. This improvement can be attributed to the reduction in strain energy release rate in the hybrid laminate, which is shown in the analysis. However, this improvement under static loading is not duplicated in fatigue test. The fatigue delamination onset is lower in the hybrid laminate than in the all-graphite laminate.

5. For S2/SP250 glass/epoxy laminates, the calculated Mode I interlaminar fracture toughness (G_{IC}) for the Mode I edge-delamination test is up to 125% higher when the thermal effects of curing are taken into account.

This Page Intentionally Left Blank.

RECOMMENDATIONS

The following recommendations are made for future research:

1. Extension of the present work to increase understanding of the failure mechanism and delamination characteristics of edge delamination in unsymmetric laminates and multiple delaminations.

2. Quantitative assessment of the effect of differences in Poisson's ratio and shear strain mismatch between two adjacent plies on delamination characteristics of laminates under tension, bending, and torsion loads.

3. Investigation of the frequency effect on fatigue delamination threshold by testing at frequencies ranging from 0.1 to 30 Hz, to cover creep at both low and high frequencies.

4. Development of an analytical model that includes the frequency effect to predict the fatigue delamination threshold.

APPENDIX

CALCULATION OF CRITICAL STRAIN ENERGY RELEASE RATE FOR THE MODE I EDGE-DELAMINATION TEST COUPON

The calculation of strain energy release rate for the Mode I edge-delamination tension test was originally derived by Whitney (1985). In reviewing his work, errors were found in equation (14) of the original paper. In this section, details of the derivation are not included. Instead, only the equations used for the calculation are presented.

The critical strain energy release rate with the residual thermal effect included can be written as follows:

$$G_{IC} = \left\{ \left[E_x \left(\varepsilon_c + \varepsilon^T \right) + T_1 \right] \left(\varepsilon_c + \varepsilon^T - \varepsilon_1^T \right) - \left[E^* \left(\varepsilon_c^f + \varepsilon^T \right) + T_2 \right] \left(\varepsilon_c + \varepsilon^T - \varepsilon_2^T \right) \right\}$$

where

$$E^* = \frac{1}{h} \left[A_{11} - \frac{A_{12}\left(A_{12} D_{22} - B_{12} B_{22} \right) + B_{12}\left(A_{22} B_{12} - A_{12} B_{22} \right)}{A_{22} D_{22} - B_{22}^2} \right]$$

$$E_x = \frac{A_{11} A_{22} - A_{12}^2}{h A_{22}}$$

$$T_1 = \frac{A_{12} N_y^T - A_{22} N_x^T}{h A_{22}}$$

$$T_2 = \frac{\left(A_{12} D_{22} - B_{12} B_{22} \right) N_y^T + \left(A_{22} B_{12} - A_{12} B_{22} \right) M_y^T}{h\left(A_{22} D_{22} - B_{22}^2 \right)} - \frac{N_x^T}{h}$$

$$\varepsilon_1^T = - \frac{T_1}{E_x}$$

$$\varepsilon_2^T = - \frac{T_2}{E^*}$$

$$\varepsilon^T = \frac{\left(T_2 - T_1\right) R + T_1}{\left(E_x - E^*\right) R - E_x}$$

$$N_i^T = \Delta T \int_{-h/2}^{h/2} \overline{Q}_{ij}^{(k)} \alpha_j \, dz \qquad (i,j = 1,2,6)$$

$$M_i^T = \Delta T \int_{-h/2}^{h/2} \overline{Q}_{ij}^{(k)} \alpha_j Z \, dZ$$

$$R = \frac{a}{b}$$

and

a = delamination length

b = half of coupon width

h = half of coupon thickness

t_i = ply thickness

$\overline{Q}_{ij}^{k}$ = k^{th} ply reduced stiffness

α_i = ply thermal coefficients

ΔT = temperature difference from stresss free condition

If the thermal effect due to curing is neglected, Eq. (A-1) can be simplified to O'Brien's equation:

$$G_{IC} = h \varepsilon_c^{\,2} (E_x - E^*)$$

REFERENCES

Armanios, E. A., and Rehfield, L. W., "Interlaminar Analysis of Laminated Composites Using a Subliminate Approach," presented in the 27th AIAA SDM Conference, May 1986.

Armanios, E. A., and Rehfield, L. W., "Interlaminar Fracture Analysis of Composite Laminates Under Bending and Combined Bending and Extension," presented at the ASTM Eighth Symposium on Composite Materials Testing and Design, April 1986.

Chan, W. S., Rogers, C., Cronkhite, J. D., and Martin, J., "Delamination Control of Composite Rotor Hubs," J. *American Helicopter Society*, August 1986.

Chan, W. S., and Ochoa, O. O., "Assessment of Free-Edge Delamination Due to Torsion," *Proceedings of the American Society for Composites*, 2nd Technical Conference, September 23-25, 1987.

Chan, W. S., and Wang, A. S. D., "A Study on the Effect of the 90° Ply in Matrix Cracks in Composite Laminates," presented in the 27th AIAA SDM Conference, May 1986.

Kassapoglou, C., and Lagace, P. A., *An Efficient Method for the Calculation of Interlaminar Stresses in Composite Materials, Part 2 - Solution Using Assumed Stresses Shapes*, TELAC Report 85-5, Technology Laboratory for Advanced Composites, Dept. of Aeronautics and Astronautics, Massachusetts Institute of Technology, March 1985.

O'Brien, T. K., "Characterization of Delamination Onset and Growth in a Composite Laminate," *Damage in Composite Materials*, K. L. Reifsnider, ed., ASTM STP 775, American Society for Testing and Materials, 1982.

O'Brien, T. K., Johnston, N. J., Morris, D. H., and Simonds, K. A., "A Simple Test for the Interlaminar Fracture Toughness of Composites," *SAMPE Journal*, Vol. 18, No. 4, July/August 1982.

O'Brien, T. K., *Mixed-Mode Strain-Energy-Release Rate Effects on Edge Delamination of Composites*, NASA Technical Memorandum 84592, NASA Langley Research Center, January 1983.

O'Brien, T. K., "Delamination Durability of Composite Materials for Rotorcraft," presented at the 1987 NASA/Army Rotorcraft Technology Conference, NASA Ames Research Center, Moffett Field, California, March 17-19, 1987.

Pagano, N. J., and Pipes, R. B., "Some Observations on the Interlaminar Strength of Composite Laminates," *Int. J. of Mechanical Science*, Vol. 15, 1973, pp. 679-688.

Pagano, N. J., and Soni, S. R., "Global-Local Laminate Variational Model," *Int. J. Solids Structures*, Vol. 19, No. 3, 1983, pp. 207-228.

Pipes, R. B., and Pagano, N. J., "Interlaminar Stresses in Composite Laminates Under Uniform Axial Extension," *J. Composite Materials*, October 1970, pp. 538-548.

Raju, I. S., and Crews, J. W., Jr., "Interlaminar Stress Singularities at a Straight Free Edge in Composite Laminates," *Computers and Structures*, Vol. 14, No. 1-2, 1981, pp. 21-28.

Rybicki, E. F., and Kanninen, M. F., "A Finite Element Calculation of Stress Intensity Factors by a Modified Crack Closure Integral," *Engineering Fracture Mechanics*, Vol. 9, 1977, pp. 931-938.

Salamon, N. J., "Interlaminar Stresses in a Layered Composite Laminate in Bending," *Fibre Science and Technology*, Vol. II, 1978, pp. 305-317.

Standard Test for Toughened Resin Composites, NASA Reference Publication 1092, revised edition, compiled by ACEE Composites Project Office, NASA Langley Research Center, Hampton, Virginia, 1983.

Wang, A. S. D., and Crossman, F. W., "Some New Results of Edge Effect in Symmetric Composite Laminates," *J. Composite Materials*, Vol. 2, 1977, pp. 92-106.

Wang, S. S., and Choi, I., "Boundary-Layer Effects in Composite Laminates, Part 2 - Free Edge Stress Solutions and Basic Characteristics," *J. Applied Mechanics*, Vol. 49, 1982, pp. 549-560.

Whitney, J. M., and Knight, M., "A Modified Free-Edge Delamination Specimen," *Delamination and Debonding of Materials*, ASTM STP 876, W. S. Johnson, ed., American Society for Testing and Materials, Philadelphia, 1985, pp. 298-314.

Ye, L., and Yang, B. X., "Interlaminar Stress Analysis in Symmetric Composite Laminates Under Bending," *Proceedings of the International Conference on Computational Mechanics*, G. Yagawa and S. N. Atluri, eds., May 25-29, 1986.

Standard Bibliographic Page

1. Report No.	2. Government Accession No.	3. Recipient's Catalog No.
NASA CR-181824		

4. Title and Subtitle	5. Report Date
An Analytical and Experimental Investigation of Edge Delamination in Laminates Subjected to Tension, Bending, and Torsion	March 1989
	6. Performing Organization Code
7. Author(s)	8. Performing Organization Report No.
Wen S. Chan	699-099-265
9. Performing Organization Name and Address	10. Work Unit No.
Bell Helicopter Textron, Inc. P.O. Box 482 Fort Worth, Texas 76101	505-63-01-05
	11. Contract or Grant No.
	NAS1-18199
12. Sponsoring Agency Name and Address	13. Type of Report and Period Covered
Langley Research Center National Aeronautics and Space Administration Hampton, Virginia 23665	Final, Jan 1986 - June 1988
	14. Sponsoring Agency Code

15. Supplementary Notes

Langley Technical Monitor: T. K. O'Brien

16. Abstract

An integrated two-dimensional finite element has been developed to calculate interlaminar stresses and strain energy release rates for the study of delamination in composite laminates subjected to uniaxial tension, bending, and torsion loads. This work addresses the formulation, implementation, and verification of the model. Parametric studies were conducted on the effect of Poisson's ratio mismatch between plies and the stacking sequence on interlaminar stress, and on the effect of delamination opening height and delamination length, due to bending, on strain energy release rate for various laminates. A comparison of strain energy release rates in all-graphite and graphite/glass hybrid laminates is included. The preliminary results of laminates subjected to torsion are also included. Fatigue tension tests were conducted on Mode I and mixed-mode edge-delamination coupons to establish the relationship between fatigue load vs. onset of delamination cycle. The effect on the fatigue delamination onset of different frequencies (1 and 5 Hz) was investigated for glass, graphite, and their hybrid laminates. Although a 20% increase in the static onset-of-delamination strength and a 10% increase in ultimate strength resulted from hybridizing the all-graphite laminate with a 90° glass ply,the fatigue onset is lower in the hybrid laminate than in the all-graphite laminate.

17. Key Words (Suggested by Author(s))		18. Distribution Statement
Composites	Fatigue onset life	Unclassified - Unlimited
Free-edge delamination	Hybrid laminate	
Finite element analysis		Subject Category 24
Interlaminar stress		
Strain energy release rate		

19. Security Classif. (of this report)	20. Security Classif. (of this page)	21. No. of Pages	22. Price
Unclassified	Unclassified	81	A05

For sale by the National Technical Information Service, Springfield, Virginia 22161